Experimental benchmark data for H-shaped and troposkien VAWT architectures

L. Battisti [a, *], G. Persico [b], V. Dossena [b], B. Paradiso [b], M. Raciti Castelli [a], A. Brighenti [a], E. Benini [a]

[a] Dipartimento di Ingegneria Civile, Ambientale e Meccanica, Università di Trento, Via Mesiano 77, I-38050, Trento, Italy
[b] Laboratorio di Fluidodinamica delle Macchine, Dipartimento di Energia, Politecnico di Milano, Via Lambruschini 4, I-20158, Milano, Italy

Most of the experimental research on vertical axis wind turbines was carried out during 1970e1980s but, recently, the potential of wind energy harvesting in new environments has renewed the interest on VAWT technology. Unfortunately, this interest still collides with an immaturity of aerodynamic model-ling tools and detailed experimental analyses are now highly recommended to convert flow field comprehension into novel design techniques.

This paper critically revises the main extensive wind tunnel campaigns conducted on VAWTs during the last 15 years. Moreover, a direct comparison between two widely adopted lift-driven rotor archi-tectures, i.e. H-shaped and troposkien, characterized by the same swept area and blade section, is pre-sented. After being instrumented to characterize aerodynamic performance and thrust as well as flow characteristics in the wake, the rotors were tested in the Politecnico di Milano wind tunnel using an open configuration, allowing real-scale measurements of micro wind turbines. A complete characterization was obtained by recording steady-state torque, thrust and flow velocity in the wake as a function of the unperturbed wind speed, while the angular velocity of the rotors was kept constant. The measurements were conducted with high accuracy and can represent a useful experimental benchmark for the vali-dation of computational tools.

Keywords: VAWT, Wind tunnel measurements, Hot wire anemometry, Turbulence measurements, Wind turbine benchmark data

1. Introduction and background

Accurate prediction of vertical-axis wind turbine (VAWT) aerodynamic performance as a function of the blade configuration is crucial for design and optimization purposes. Nevertheless, due to the fully three-dimensional flow characteristics and to the double interaction between the blade and each streamtube in a complete revolution, the computational simulation of the flow around VAWTs is still a challenging task. A significant development of computational techniques for simulating the wind energy con-version physic has recently been registered, starting from the earliest actuator disc theory [1] up to the single [2] and double [3,4] multiple-streamtube blade element momentum (BEM), vortex methods [5] and computational fluid dynamics (CFD) codes [6–12]. Nevertheless, the effectiveness of rotor aerodynamic design ultimately relies on the fidelity to reality of the chosen mathe-matical model [13]. As a consequence, the availability of experi-mental benchmarks appears to gain the utmost importance to complement and support validation and calibration of computa-tional codes; at the same time, detailed experimental in-vestigations are highly recommended to convert improved flow field comprehension into novel design techniques.

The vertical axis architecture is characterized by a shaft perpendicular to the incoming flow, that allows handling rapid fluctuations in wind direction and makes it suitable for highly variable and turbulent installation sites. Thanks to a relatively low peripheral velocity of the blades with respect to other wind turbine technologies, such configuration is generally characterized by a low noise emission, which is highly desirable for urban installations. On the other hand, VAWTs are often incapable of self starting, requiring an initial rotation (that must be supplied from the outside) to generate the aerodynamic loads on the blades.

The majority of experimental research on VAWT design was carried out during late 1970s and early 1980s. Successively, interest

Article history:
Received 11 August 2017
Received in revised form 29 December 2017
Accepted 18 February 2018
Available online 21 February 2018

* Corresponding author.
E-mail address: lorenzo.battisti@unitn.it (L. Battisti).

© 2018. This manuscript version is made available under the CC-BY-NC-ND 4.0 license http://creativecommons.org/licenses/by-nc-nd/4.0/
Published Journal Article available at https://doi.org/10.1016/j.renene.2018.02.098

in VAWTs faded and horizontal-axis wind turbines (HAWTs), whose axis is aligned to the direction of the incoming wind, have since dominated all current large scale wind farms [14] and today represent the major portion of worldwide installed capacity [15]: this was due to their higher aerodynamic performance with respect to their vertical axis counterparts, even though they are unable to handle rapid variations of the incoming wind direction, that should ideally always be perpendicular to the rotor disc. As a result, very few experimental investigations on VAWT aerodynamics can be found during the last couple of decades, determining a significant lag in literature benchmark data with respect to classical HAWT designs, such as [16].

From a literature survey, Sandia Laboratories (USA) first focused on VAWT open field measurements [17–21], while only a few tests were performed using wind tunnels [20,22]. Unfortunately, detailed aerodynamic measurements cannot be achieved through open field testing, due to the inevitable disturbance of the surrounding environment. Moreover, in most cases, some fundamental test conditions (such as wind shear or flow turbulence) are not clearly stated, raising some doubts when dealing with the boundary conditions to be applied at numerical codes during the validation phase.

Despite some recent campaigns focused on wind tunnel testing of vertical-axis rotors, too high geometric blockage factors (> 10%) were often used, clearly determining an alteration of flow characteristics at the test section due to a too large obstruction from the rotor itself. Generally speaking, wind tunnel boundaries (consisting in both solid walls or a jet boundary in an open jet wind tunnel, see also [23]) impose such an important constraint on the flow field around the tested model that measured parameters can dramatically differ from open field operation: even though some correction factors where derived for HAWTs [24–26], the extension of such models to VAWTs is still an open issue (in particular, the work of Battisti et al. [27] and Dossena et al. [28] clearly highlighted that the presently available theoretical correction models do not provide accurate estimates of the blockage in the case of VAWTs). Moreover, it is always hard to clearly define the frontal area of a spinning rotor (the frontal area of a stationary rotor is quite small, conversely the swept area of a spinning one is quite high): of course, the most conservative computation of the blockage ratio is based on the swept (frontal) area of the rotor.

Table 1 shows a summary of the main extensive wind tunnel experimental campaigns conducted on VAWTs during the last 15 years: measured flow turbulence (if available) is highlighted, as well as the 3D geometric blockage (declared by authors or estimated), computed as:

$$\varepsilon = \frac{A_s}{W_{wt} H_{wt}} \tag{1}$$

It is clearly found that only a handful of works did succeed in respecting blockage ratios below about 10–15% (registering values up to 61% in the case of [29]), thus determining potential errors in the measured power performance of the rotor, unfortunately biased towards the optimistic side; moreover, with the only exception of [27,28,30], no attempt was made to correct the blockage using available models from literature. Whilst this issue could be considered irrelevant when comparing measured data to CFD simulations (thanks to their capability of reproducing the whole measurement environment, implementing also the tunnel surfaces as boundary conditions), it would affect the comparison with other generally accepted simulation tools such as BEM models, as well as extrapolation to real operating conditions.

It can also be observed that the turbulence level at the entrance of the test section (i.e., the level of unsteady velocity fluctuations

Table 1
Summary of the main extensive wind tunnel campaigns conducted on VAWTs during the last 10 years; ([1]): only for open jet wind tunnel configurations; ([2]): not applicable due to only vortices visualization; ([3]): estimated by comparison with other articles; ([4]): not applicable due to only wake measurements.

Ref.	*Year*	*Wind tunnel configuration*	*Test section location with respect to upstream wind tunnel outlet* [m] ([1])	*ε*[%]	*Blockage correction*	*I*[%]	*Spoke geometry*	*First spoke position (frombladetip)*[%]	$Re_c[-]$	*Elimination of bearing losses*
Van Bussel et al. [31]	2004	open jet	NA	14	no	NA	NA	NA	5.0E+04	no
Van Bussel et al. [31]	2004	open jet	NA	43	no	NA	NA	NA	1.5E+05	no
Ferreira et al. [32]	2006	open jet	NA	10	no	1.2–1.7	NA	25	1.2E+05	no
Ferreira et al. [33]	2007	closed test section	–	18	no	<0.1	NA	15	5.0E+05 and 7.0E+05	- ([2])
Tullis et al. [34]	2008	closed test section	–	9	no	NA	NA	25	5.5E+05	no
Fiedler and Tullis [35]	2009	open jet	8	19	no	NA	NA	25	4.4E+05	yes
Takao et al. [36]	2009	open jet	1.2	17	no	NA	NA	NA	9.0E+04	no
Howell et al. [14]	2010	closed test section	–	17	no	1 ([3])	NA	0	7.5E+04	yes
Li et al. [29]	2010	open jet	0.5	61	no	NA	NA	50	3.5E+04	yes
Battisti et al. [27]	2011	both open jet and closed test section	NA	10	yes	<1	NA	NA	1.5E+05	- ([4])
Armstrong et al. [37]	2012	open jet	8	22	no	NA	NA	NA	5.0E+05	no
Danao et al. [38]	2013	closed test section	–	29	no	1	yes	25	5.0E+04	yes
Li et al. [39]	2014	open jet	2.06	24	no	NA	NA	NA	2.5E+05	no
Tescione et al. [40]	2014	open jet	NA	14	no	<0.5	yes	20	1.3E+05 and 2.1E+05	- ([4])
Dossena et al. [28]	2015	both open jet and closed test section	NA	10	yes	<1	NA	NA	1.5E+05	yes
Peng et al. [41]	2016	open jet	6	1.8	no	2.5	no	NA	2.5E+04	- ([4])
Battisti et al. [30]	2016	open jet	2.04	17	no	<1	yes	yes	1.4E+05 and 2.5E+05	yes

about the flow average velocity) is seldom declared by authors (for a recent comprehensive investigation on how turbulence can affect the power curve of a wind turbine, the reader is referred to [42]): also such issue prompts several concerns about both reliability and repeatability of those measurements.

Furthermore, the complete geometry of spokes is never clearly stated (not even their exact position with respect to blade tip, in the case of [31,36,37,39]), except for some vague descriptions such as "profiled cross bars" [32], "streamlined steel struts" [35], "aerodynamically profiled with an elliptical leading edge and sharp trailing edge" [14] and "streamlined aluminium extrusions" [37]. A sufficiently clear technical description of the spokes is provided in Ref. [40] only, even though the paper does not report explicitly the coordinates. Unfortunately, it is definitively recognized that spoke drag affects significantly the power performance of H-shaped rotors (for a recent numerical investigation on the influence of spokes on overall rotor performance, see Ref. [43]): as a consequence, a complete modelling of spoke geometry should be required to correctly calibrate any numerical model.

Moreover, just a few works [14,29,30,35,38] account for the contribution of bearing losses on the measured power performance of the tested rotor. Also the location of the test section (i.e. normal to the incoming flow and containing the rotor axis of revolution) with respect to the upstream outlet of the wind tunnel (for open jet configurations) is sometimes missing [31,32], thus raising some doubts about the correct definition of the external simulation domain, for instance in case of CFD code validation.

Finally, it should be observed that, probably with the aim of reducing the distorting effects of wind tunnel blockage, some measurements were performed using very small rotor arrangements ($R_{eq} = 0.15$ m [29], $R_{eq} = 0.3$ m [31], $R_{eq} = 0.35$ m [38], $R_{eq} = 0.3$ m [41]), thus leading to unrealistic chord Reynolds numbers (respectively $Re_c = 5.0E+04$, $Re_c = 3.5E+04$, $Re_c = 5.0E+04$, and $Re_c = 2.5E+04$ with $Re_c = \Omega R_{eq} c/\nu$).

All of the above taken into account, it appears evident that the efforts provided during the last 15 years to obtain new accurate VAWT experimental benchmark data are still insufficient. The hereby proposed work aims at filling such gap by presenting the results of an experimental campaign conducted in low turbulence (controlled) conditions, with the ambition of setting the benchmark for three-dimensional simulation of VAWT aerodynamics and performance by providing validation test cases for the two most common rotor architectures (H-shaped and trospokien).

To this end, the presented experimental measurements include aerodynamic power and thrust (in both longitudinal and transversal directions), as well as flow velocity in the wake, over a wide range of operating conditions. In order to have a fair comparison, the two tested rotors are characterized by the same swept area and blade profile. While presenting the results in non-dimensional form, thus allowing a direct comparison between the two candidate rotor configurations, also raw data are provided in tabular form, with the aim of making the proposed benchmark immediately available to researchers for the validation of numerical codes.

2. Experimental set-up

This section reports a detailed description of the experimental setup, consisting in the low turbulence and large scale wind tunnel facility (Section 2.1), the two tested rotors (2.2) and the measurement systems (2.3).

2.1. Wind tunnel facility

The hereby proposed measurements were taken at the large scale, high-speed wind tunnel of the Politecnico di Milano (Italy): it consists of a closed-loop facility whose test section (4.00 m wide, 3.84 m high and 6.00 m long) allows the aerodynamic characterization of micro-wind turbines up to 55 m/s, thanks to 2 rows of 7 electric driven fans, each of them controlled by an independent inverter, for an overall installed capacity of approximately 1.4 MW. Tests were carried out using a "free jet" (open) configuration, by removing the test room and installing the rotors directly facing the upstream tunnel, as shown in Figs. 1 and 2. High flow quality was assured by a combination of honeycombs and anti turbulence screens, with a measured freestream turbulence intensity (at the inlet of the open test section) lower than 1%. These are of course ideal operating conditions (steady and spatially uniform wind, low turbulence level) and the real operating behaviour of the rotors is expected to be different, unavoidably plagued by the turbulence of the installation site. On the other hand, controlled flow conditions are essential for the validation of computational tools. For a deeper understanding of the effect of turbulence on the power curve and to extend the here derived performance curves to field operations, the interested reader is referred to [42].

In order to provide a complete set of geometrical boundary conditions for numerical code validation, Fig. 3 and Table 2 show a quoted scheme of the open test section and of both the H-shaped and troposkien installations.

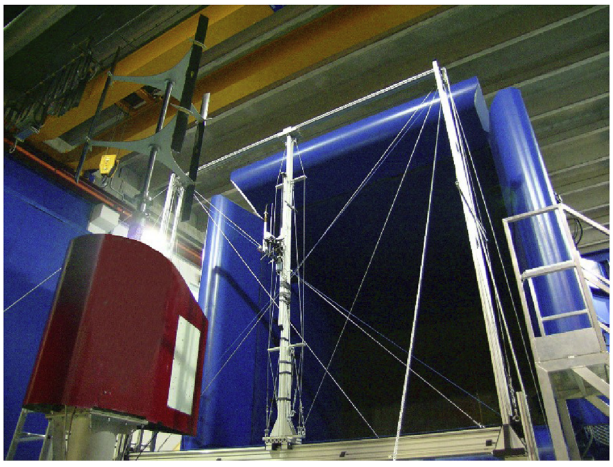


Fig. 1. Bottom view of the open chamber, showing the H-shaped rotor mounted on top of the test bench; the traversing system for wake measurement is visible downstream of the test bench.

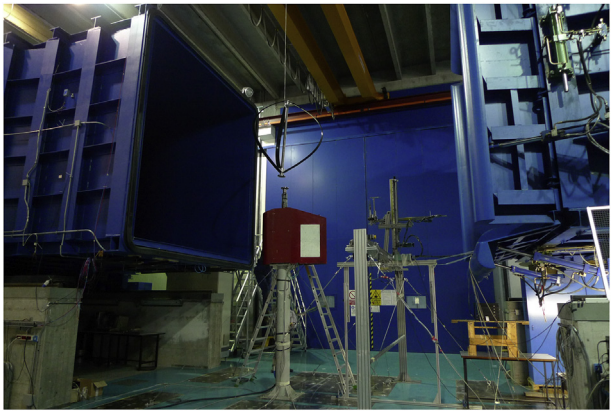


Fig. 2. Side view of the open chamber while positioning the troposkien rotor; the traversing system is also visible downstream of the test bench.

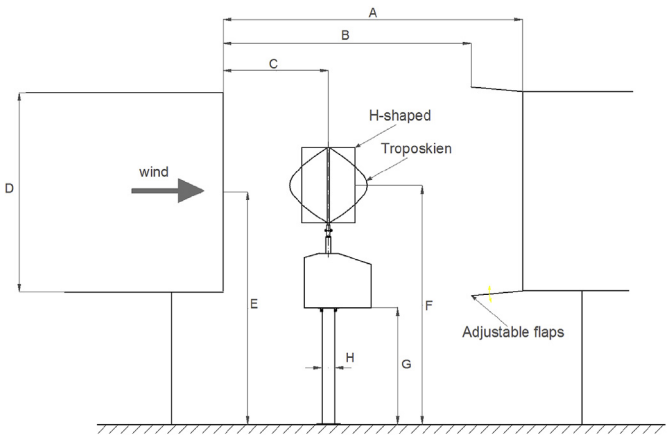


Fig. 3. Scheme of the experimental facility and rotor set up.

Table 2
Main dimensions (in mm) of the open test section and of rotors installation (Fig. 3).

Ref.	*Dimension* [mm]
A	5800
B	4800
C	2040
D	3840
E	4500
F	4624
G	2262
H	250

2.2. Tested turbine architectures

Table 3 reports the common features of the two tested rotors (H-shaped and troposkien), characterized by the same swept area (the resulting 3D geometric blockage ε is less than 10%) and number of blades (3), in order to provide a fair comparison. The tested rotors (Fig. 4) share also the same blade section (NACA 0021) and manufacturing technique (resin infusion molding of carbon fibers reinforced plastic).

According to the Merker and Wiedemann model for non rotating bluff bodies, adapted as proposed in [28], a quantification of the open-jet blockage was performed. Despite having the same swept area, rotors unlike aspect ratio influence the flow patterns in different ways: the H-shaped and Troposkien rotors yield, respectively, a blockage correction coefficient of 1.5% and 2.1%. This result means that a little lower measured wind speed would be required to recover the open field conditions. However, no blockage correction was applied to the present data, because such correction is very small and comparable to the wind speed measure uncertainty.

2.2.1. H-shaped rotor

Table 4 and Fig. 5 summarize the main geometric features of the H-shaped rotor, as well as mass and inertial properties. In order to allow also the complete rotor modelling, the coordinates of the reference spoke (i.e. aligned along the y axis) are provided by Table 5 in the Appendix. The second spoke and the third one can be easily modeled through a rotation (respectively by 120° and 240°) of the first one around the vertical axis z (see Fig. 22 in the Appendix). As shown in Figs. 4 and 5, two set of spokes are placed along the blades: one in the upper part of the rotor, and another one in the lower part.

2.2.2. Troposkien rotor

The troposkien architecture is characterized by hub-to-hub blades, resulting in a much cleaner rotor design (leading to a reduction of blade tip effects) and a lower polar inertia than the corresponding H-shape configuration. Moreover, thanks to the elimination of non-aerodynamic spokes (at least for small-scale VAWTs, where structural constraints are less demanding) the troposkien architecture offers a lower aerodynamic drag (compared to the H-shaped one).

Table 5 and Fig. 6 summarize the main geometric features of the Troposkien-shaped rotor, as well as mass and inertial properties. Table 7 in the Appendix summarizes the cylindrical coordinates of the troposkien rotor blade.

2.3. Measurements and data reduction

All the presented measurements were performed at constant nominal rotational speed ($\Omega_n = 400$ rpm) and by varying the freestream wind velocity (from 6.09 m/s to 16.18 m/s for the H-

Table 3
Common features of the two tested rotors.

A_s [m^2]	*Blade number*	*Blade profile*	c [mm]
1.5	3	NACA 0021	85

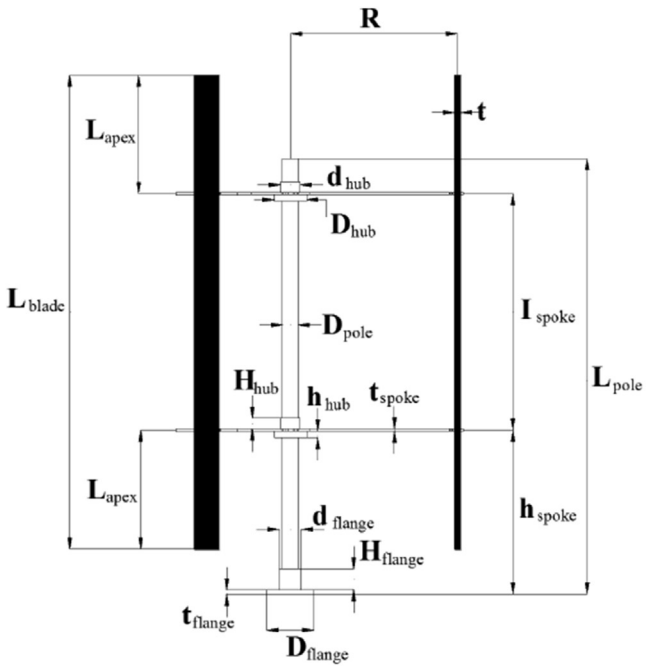
Table 4
H-shaped rotor main geometric features (see Fig. 5), mass and inertial properties.

R [mm]	t [mm]	L_{blade}[mm]	*Solidity*[−]	Mass[kg]	*Polar inertia*[kgm^2]
514	18	1460	0.25	26	1.5



(a) side view (b) top view

Fig. 4. H-shaped (left) and troposkien (right) tested rotors.



	[mm]
L_{apex}	366
L_{pole}	1367
D_{pole}	50
s_{pole}	10
I_{spoke}	727
h_{spoke}	49.8
t_{spoke}	6.3
D_{hub}	100
d_{hub}	60
H_{hub}	33.8
h_{hub}	20
D_{flange}	150
d_{flage}	70
H_{flange}	87
h_{flange}	15

Fig. 5. Quoted drawing (in mm) of the H-shaped rotor.

Table 5
Troposkien-shaped rotor main geometric features (see Fig. 6), mass and inertial properties.

R [mm]	t [mm]	L_{blade}[mm]	H [mm]	*Solidity*[−]	Mass[kg]	*Polarinertia*[kgm^2]
755	18	2.233	1.510	0.38	18	0.5

shaped rotor and from 3.15 m/s to 20.01 m/s for the troposkien one). The rotational speed was kept constant during the test by an inverter-controlled electrical machine.

2.3.1. Thrust and performance measurement system

Rotor torque and thrust measurements were performed using a high accuracy test bench (see Fig. 7, representing the H-shaped rotor set up), which was instrumented using the following calibrated sensors:

- 2 strain gauge bridges, installed on the supporting mast, to measure both longitudinal (X) and transversal (Y) aerodynamic thrusts;
- an absolute encoder, to provide both rotational speed and rotor phase (i.e. the azimuthal position of the reference blade);
- a torquemeter, mounted between elastic joints, to measure the mechanical torque at rotor shaft.

A smooth hull was positioned around the measurement train (see again Fig. 7 - right) to reduce the solid blockage. Fig. 7 (left) also provides both plan and side views of the hull shape, thus allowing a complete numerical modelling of the experimental set up. The data acquisition system was placed inside the hull and connected by a LAN cable to the control room.

A sampling frequency of 2000 Hz (2 kSa/s) was achieved by means of a Compact-RIO (National Instruments). While instantaneous (local) aerodynamic data were registered as a function of time, averaged (over a full revolution) torque and thrust were obtained registering 3 min long time series for each rotor operating condition. The data reduction was successively determined by:

- dividing each time series into 20 s bins (i.e., each 3 min record was divided into 6 bins, each comprising the mean value and the standard deviation (which provides information about the unsteadiness of the flow field);
- computing both power and thrust curves starting from the average values deriving from each bin;
- deriving the standard deviation from the average bin values.

Measurement errors (category A and B uncertainties) were computed according to ISO ENV 13005 [44] for a confidence interval of 95%, as well as the error propagation for derived measurements.

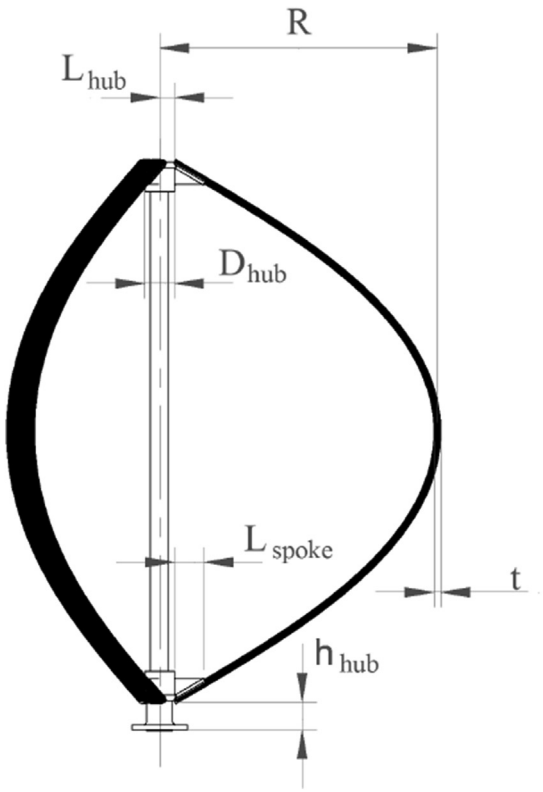
The whole system (i.e. wind tunnel, tested rotor and instrumented test bench) was set off every three measured working conditions to record sensor offsets. To estimate the inverter-converter electromagnetic noise, offsets were measured with the controller switch on: the resulting mean noise added to sensor readings was negligible.

The data acquisition system provided rough data, converted from voltage or current to the desired quantities, such as bending moment, mechanical torque and rotational speed. A further data processing was performed to obtain other quantities, such as rotor thrust (here assumed as acting at rotor midspan), gross aerodynamic torque and power, as well as the corresponding normalized coefficients.

Bearing losses were measured by fastening a cylindrical steel (characterized by a mass equal to the corresponding rotor) to the test stand and then measuring the mechanical torque (from 50 rpm to 600 rpm, using a 50 rpm step). The resulting value was successively added to the measured aerodynamic torque. Power was computed as the product of aerodynamic torque and angular speed.

2.3.2. Flow measurement system

To investigate the velocity field and the turbulence structures in



	[mm]
R	755
D_{hub}	80
L_{spoke}	81
h_{hub}	75
L_{hub}	41

Fig. 6. Quoted drawing (in mm) of the troposkien rotor.

Table 6
Zero wind drag coefficient C_{D0} measured at 400 rpm.

	Q_{aero} [Nm]	C_{D0} [−]	Re_c [−]
Troposkien-Darrieus	1.66	0.0025	174 350
H-Darrieus	1.77	0.0085	118 500

the wake, two single-sensor hot wire probes were traversed on several measurement surfaces downstream of the rotors.

Tungsten wires of 5 μm diameter were used, operated in constant temperature mode to ensure high bandwidth, largely exceeding the harmonic content of the velocity signals measured in the present study (the blade passing frequency is 20 Hz). The velocity signals were acquired in each point of the measurement

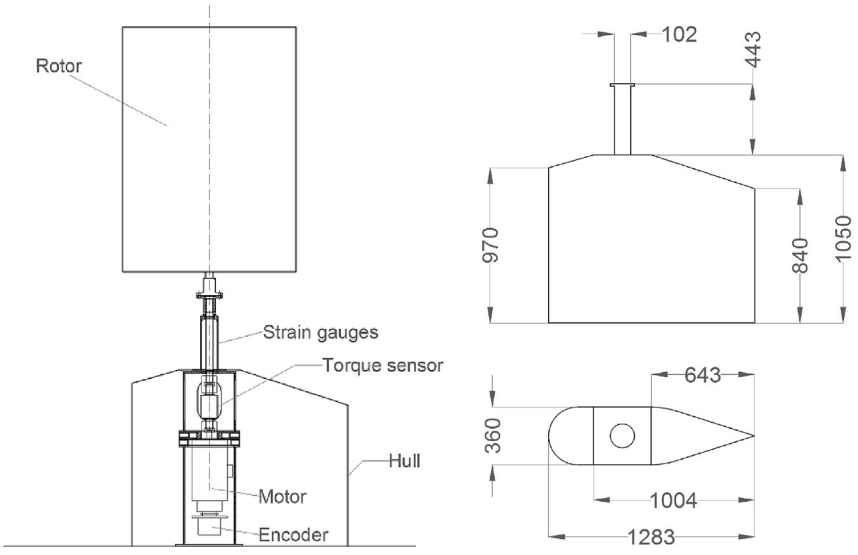


Fig. 7. Set up of the test bench instrumentation (left) and quoted views of the hull (right) in mm.

surfaces for 2 s with a sampling frequency of 40 kHz. Measurements did not show any significant harmonic content above 200 Hz; to minimize the impact of measurement noise, the raw voltage signals were low-pass filtered at the same frequency. Uncertainty in the velocity measurements resulted about 2% after calibration in a low speed jet for both the sensors. The first hot wire probe was mounted aligned with the longitudinal (X) direction, exposing the wire orthogonal to the wind (i.e., along the transversal, or Y, direction). For measurement assessment, a second hot wire probe was mounted in axial (Z) direction, exposing the wire orthogonal to the wind (i.e., along the Y direction); this second hot wire was further rotated around its own axis by ±45° with respect to the Y direction to measure the streamwise as well as cross-stream velocity components. Preliminary analyses indicated the presence of slight cross-stream flow components in the wake, even though remaining within the range of insensitivity of both the first and second hot wires (the latter, of course, when aligned along Y); this allows to consider the hot wire recordings as direct measurements of the velocity magnitude.

To extract synthetic information on the wake character, the velocity measurements were processed with a dedicated technique. At first, the so-called triple decomposition was performed to decouple the deterministic unsteadiness promoted by the motion of the blades from the unresolved unsteadiness, that can be correlated to turbulence. In the wake of a turbine rotor the velocity magnitude measured by the hot wires can be written as the combination of the time-averaged component V_{TM}, the phase-resolved component V_{PER}, and the streamwise turbulent component V_{TU}:

$$V(t;X,Y,Z) = V_{TM}(X,Y,Z) + V_{PER}(t;X,Y,Z) + V_{TU}(t;X,Y,Z) \tag{2}$$

The time-mean velocity component was computed as simple arithmetic average of all the samplings available. The periodic and turbulent components were computed by resorting to ensemble averaging, after having subtracted the time-mean datum. The velocity signals were first phased-locked on the rotor wheel, by using the encoder mounted on the rotor as key-phasor; the periodic component was then calculated by averaging among values pertaining to the same phase for all the blade passing periods acquired in each measurement record. Finally the instantaneous turbulent component was determined by subtracting the periodic and time-mean components to the instantaneous velocity signal.

On the basis of the aforementioned decomposition, two statistics were applied. At first, the root-mean-square of the periodic velocity component was computed, made non-dimensional by using the freestream wind speed and named I_{PER} in the following. The quantity I_{PER} measures synthetically the intensity of the periodic fluctuations of the velocity and, hence, marks the regions of the wake affected by the deterministic unsteadiness. The root-mean-square of the streamwise turbulent component was also computed and divided by the freestream wind speed, thus obtaining the turbulence intensity I_{TU} pertaining to the streamwise turbulent component.

In this paper, these synthetic quantities are plotted alongside the mean velocity profile in the wake to highlight the character of the wake unsteadiness for the two rotors in several operating conditions.

In addition to velocity measurements, pneumatic measurements were also performed in the wake by applying a directional five-hole probe, thus obtaining the time-mean total and static pressure fields and the time-mean three-dimensional velocity vector. The probe was calibrated on a low-speed jet over an angular range of ±24 deg in both the flow angles. Uncertainty in pressure measurements resulted within 10 Pa, while that on the flow angle ones resulted ±0.2 deg. The flow angle distribution constructed by combining the time-mean streamwise and the cross-stream velocity components measured with the hot wire was found to be in good agreement with the one measured by the five-hole probe.

3. Results and discussion

3.1. Rotor performance and thrust measurements

Measured mean data for the two tested rotor architectures are summarized in Tables 8 and 9 in the Appendix: freestream wind velocity at the test section inlet, ambient temperature and corresponding air density, nominal and measured rotor angular speeds, aerodynamic torque and thrusts in both longitudinal (X) and transversal (Y) directions are here presented along with the connected uncertainties. The resulting maximum Re^+ and minimum Re^- blade Reynolds numbers, respectively defined as:

$$\begin{aligned} Re^+ &= \frac{(\Omega\, R_{eq} + V_0)c}{\nu} \\ Re^- &= \frac{(\Omega\, R_{eq} - V_0)c}{\nu} \end{aligned} \tag{3}$$

are also reported, whereas the blade chord Reynolds numbers Re_c for the H-shaped and troposkien rotor configurations are respectively 1.2E+05 and 1.7E+05 (also in this case at the maximum, equatorial, radius R_{eq}). Due to the variable distance from the rotational axis of the troposkien rotor sections (from very low values of both upper and lower blade stations to much higher values of the midspan ones), the mean chord Reynolds number (i.e. averaged along the blade) is quite close to the one of the H-shaped architecture.

Fig. 8 shows the power curves as a function of wind speed for both rotors: as can be clearly seen, typical stall power curves are obtained. A quite similar behaviour is registered for low wind velocities and a cut-in wind speed of 6–6.5 m/s is observed. As a matter of fact, VAWTs with fixed pitch blades are unable to start autonomously: rotor self starting capability was investigated by Refs. [45–47] and it is promoted by the blade camber, thickness and rotor solidity. The symmetrical NACA 0021 profile, adopted for the presented rotors, is relatively thick and it is reasonable to assume

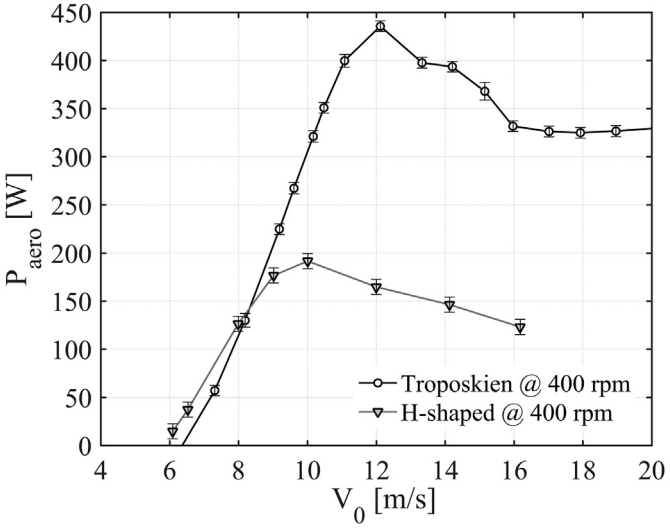


Fig. 8. Power curves for the two analysed rotor configurations.

that it could reduce the severity of the negative torque region at low wind speeds, but this still remains an open issue.

As wind speed increases (over about 8.5 m/s) a higher power extraction of the troposkien configuration is clearly visible (Fig. 8). This should be ascribed to the reduction of both blade tip losses (induced drag) and parasitic drag due to spokes. As a matter of fact, as Fig. 4 clearly represents, for the small VAWTs the "eggbeater"-shaped architecture permits to avoid non-aerodynamic spokes, contrary to the H-shape configuration. It should also be noted some delay in the stall behaviour of the troposkien rotor (see again Fig. 8). Even though further investigation should be performed to better clarify this quite different behaviour, it could possibly be connected with the higher equatorial blade Reynolds number, which promotes an improved aerodynamic efficiency. It is here just recalled the higher equatorial radius of the troposkien rotor ($R_{eq} = 755$ mm) with respect to the H-shaped configuration ($R_{eq} = 515$ mm), in order to maintain the same rotor swept area. For this reason, during operation at 400 rpm, 50% of the central part of the Troposkien rotor works with local Re_c larger than that registered for the H-shaped rotor.

An interesting feature is observed for the post-stall region: in Fig. 8 a self-limitation of the troposkien rotor is observed, in particular at 70% of the peak power, starting from 16 m/s.

The present experiments clearly demonstrate how complex is the comparison between VAWTs of different architecture: contrarily to the case of the aerodynamic power, quite similar thrust values are experienced by the two tested architectures. Fig. 9 shows the measured thrusts in both longitudinal (X) and transversal (Y) directions. This results seem to indicate that the same rotor swept area, blade section and rotational speed drive to similar aerodynamic thrusts, despite the different rotor architectures and power harvest.

Figs. 10 and 11 report about the rotor aerodynamic performance, showing the normalized coefficients of power and thrust, defined as:

$$C_{P,\,aero} = \frac{P_{aero}}{0.5\,\rho\,A_s\,{V_0}^3} \tag{4}$$

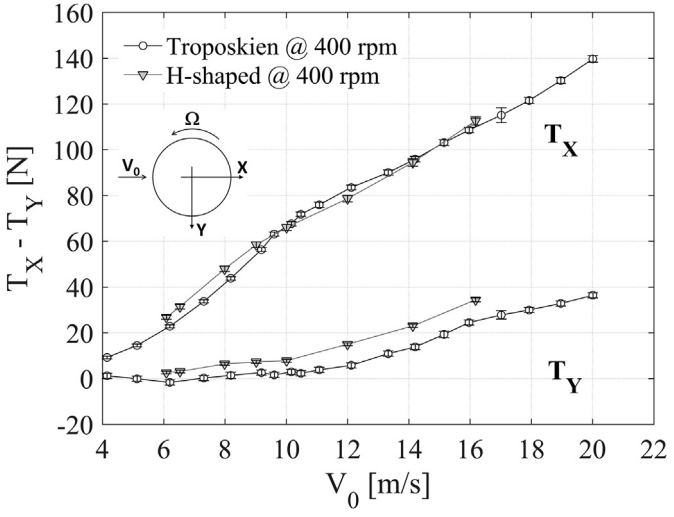


Fig. 9. Longitudinal (X) and transversal (Y) thrusts for the two analysed rotor configurations.

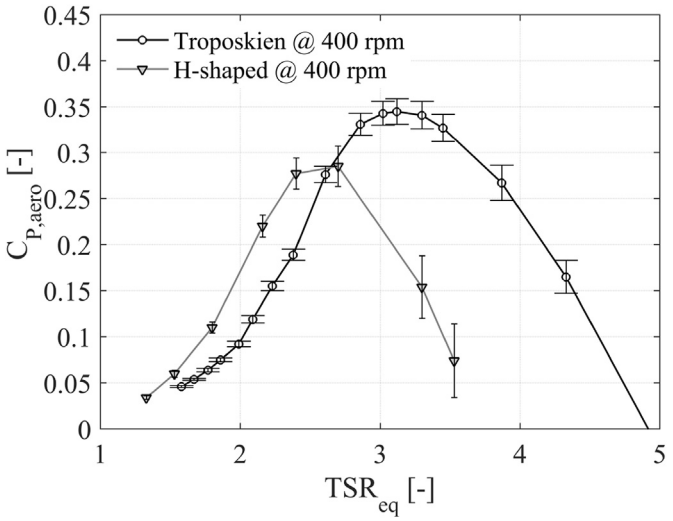


Fig. 10. Rotor power coefficients, eqn. (4), as a function of the equatorial tip speed ratio, eqn. (6).

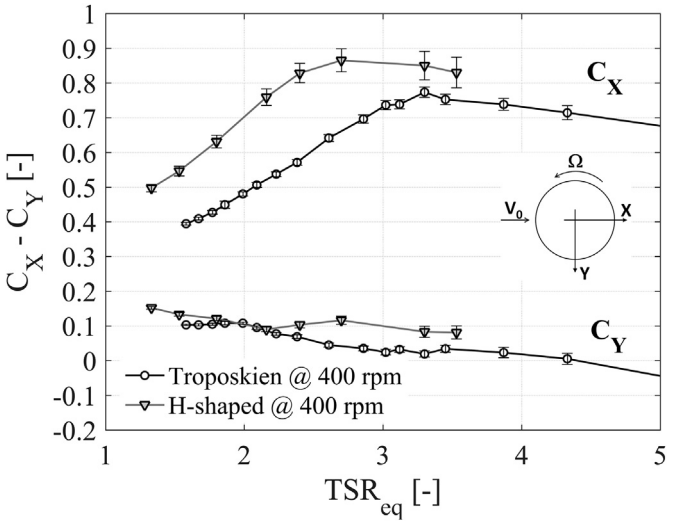


Fig. 11. Rotor longitudinal and transversal thrust coefficients, eqn. (5), as a function of the equatorial tip speed ratio, eqn. (6).

$$C_X = \frac{T_X}{0.5\,\rho\,A_s\,{V_0}^2} \qquad C_Y = \frac{T_Y}{0.5\,\rho\,A_s\,{V_0}^2} \tag{5}$$

as a function of the equatorial tip speed ratio, in formula:

$$TSR_{eq} = \frac{\Omega\,R_{eq}}{V_0} \tag{6}$$

being R_{eq} the radius of the H-shaped rotor or the equatorial radius of the troposkien one. Rotor *solidity* for Darrieus VAWTs is defined by Sandia Laboratories (see Ref. [22]) as:

$$\sigma = \frac{N\,c\,L}{A_s} \tag{7}$$

The different blade length is responsible of the fact that the H-shaped rotor solidity (0.25) results lower than the troposkien-

shaped one (0.38). The higher rotor solidity of the troposkien turbine should be reflected in the C_P-TSR_{eq} curve (Fig. 10), placing the troposkien curve on the left side of the H-shaped one [22]. On the contrary, the measures collected in Fig. 10 show a different behaviour, exhibiting the prevalent effect of the turbine drags: the blade and spoke (when this is present) shape, the blade Reynolds number, the quality of the blade manufacture, etc. are all geometrical and aerodynamic variables which help in giving a different overall rotor drag and, thus, efficiency during the turbine operation. In the present wind tunnel campaign, the C_{D0} (i.e. the drag coefficient experienced by the rotor when it is powered at zero wind speed) was measured as:

$$C_{D0} = \frac{Q_{aero}}{0.5\,\rho\,A_s\,(\Omega\,R_{eq})^2 R_{eq}} \tag{8}$$

The value of C_{D0} expresses a measure of the turbine aerodynamic loss and, in the present case, it highlights the effect of chord Reynolds number [48]: high values of C_{D0} result in low values of C_P, displacing the C_P peak at lower TSRs. Table 6 reports the C_{D0} measured at 400 rpm; the great difference between H-shaped and troposkien data should be mainly ascribed to the spokes parasitic drag, as mentioned before.

It should also be observed that, due to the choice of presenting normalized data with respect to the equatorial tip speed ratio (TSR_{eq}), the resulting peaks in power (Fig. 10) and thrust coefficients (Fig. 11) of the troposkien rotor are at higher TSR_{eq} than the corresponding values of the H-shaped architecture. The Authors recognize that the hereby presented measurements could have also been performed by lowering the angular velocity of the troposkien rotor, in order to maintain (at its equatorial section) the same peripheral speed of the H-shaped configuration. Nevertheless, it should be reminded that the local tip speed ratio of troposkien architectures varies with continuity from rotor upper tip sections (where the minimum value is registered) to its equatorial plane: as a consequence, no unique tip speed ratio can be defined for troposkien architectures.

Thrust coefficients in both longitudinal (X) and transversal (Y) directions are shown in Fig. 11. These data reflect the measured thrusts reported in Fig. 9, emphasizing the load differences recorded at high TSR_{eq} (low wind speeds).

3.2. Wake measurements

The experimental characterization of the wake shed by wind turbines provides key information on both the rotor aerodynamic behaviour and the disturbances induced in the downstream flow by the machine operation, also with regard to the application in wind farms. The wake analysis is particularly relevant for VAWTs, in which the blade profiles operate in continuously varying flow conditions during their circular trajectory. As a result, VAWT wakes exhibit a very complex character, and their accurate investigation is instrumental to shed some light on the local aerodynamic processes occurring in the rotor. Furthermore, the accurate prediction of the wake downstream of VAWTs with both simplified engineering models and advanced CFD tools is extremely challenging due to the fully unsteady aerodynamics of the rotor and the potential onset of dynamic stall on the aerofoils. For these reasons, an experimental benchmark on VAWTs cannot leave aside a comprehensive analysis of the wake in combination to the overall force and performance measurements presented in the previous Sections.

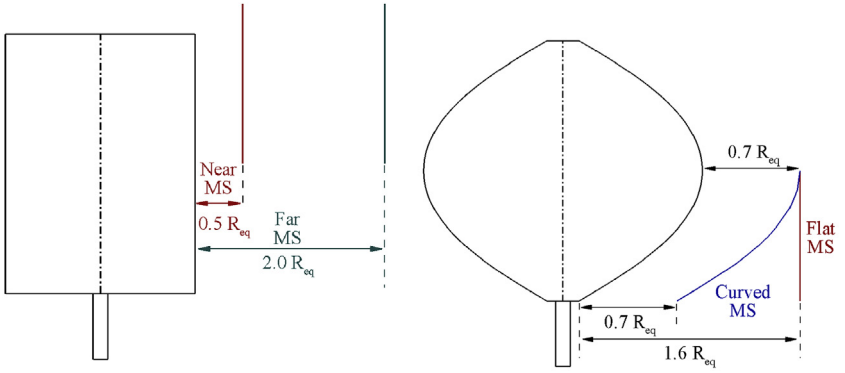
In this work, the wake shed by the two Darrieus turbines were experimentally investigated by means of velocity measurements performed on several surfaces downstream of the rotors; the probes were traversed by using a three-dimensional system featuring three independent and computer-controlled actuators, specifically designed and manufactured for the present experimental study.

The wake of the H-shaped rotor was investigated on two flat surfaces, schematically shown in Fig. 12(a):

- the *near MS*, placed at 0.5 R_{eq}, or 0.257 m, downstream of the virtual cylinder swept by the blades;
- the *far MS*, placed at 2.0 R_{eq}, or 1.028 m, downstream of the virtual cylinder swept by the blades.

The measurement grids were composed by almost 200 points (23 transversal x 8 vertical) and, as visible in Fig. 12(a), they covered the upper half of the turbine only (thanks to the symmetry of the rotor geometry) and were extended above the tip to properly capture the flow phenomena in this area. The name given to the traverses has both 'geometric' and 'physical' meaning. As a matter of fact, the *near MS* is indeed very close to the rotor, so to capture the evolution of the flow in the near wake of the machine. The *far MS* is instead distant enough from the rotor so to have a complete pressure recovery in the wake (in the limit of the measurement uncertainty of the five-hole probe); hence, the flow measured there can already be considered representative of the far wake.

The wake of the troposkien turbine was investigated on two very different traverses, schematically shown in Fig. 12(b),



(a) H-shaped turbine measurement surfaces (b) Troposkien turbine measurement surfaces

Fig. 12. Side view of measurement surfaces for H-shaped and troposkien turbine test campaigns.

conceived to investigate the development of the wake with two different perspectives:

- a conventional flat traverse, called *flat MS*, placed at 0.70 R_{eq}, or 0.53 m, downstream of the virtual troposkien solid of rotation swept by the blades in the equatorial section;
- a curved measurement surface (in the X-Z plane), called *curved MS*, designed to keep the probes at a constant distance of 0.53 m from the virtual troposkien solid of rotation swept by the blades along the whole turbine axis.

In this case, the grids were composed by almost 300 points (23 transversal x 12 vertical) and, as visible in Fig. 12(b), they covered the lower half of the turbine only (thanks to the symmetry of the rotor geometry). They were tapered towards the rotor tip to improve the resolution where the rotor diameter reduces.

In the following the mean flow velocity, as well as the statistics performed on both the deterministic and turbulent unsteadiness of the flow velocity, are shown and discussed. The experimental results are reported in the form of V/V_0 and I_{TU} profiles along the transversal (Y) direction. To better highlight the relevance of the deterministic unsteadiness with respect to the local flow velocity in the wake, the local value of I_{PER} along the transversal coordinate is represented as error bar over the mean velocity profile.

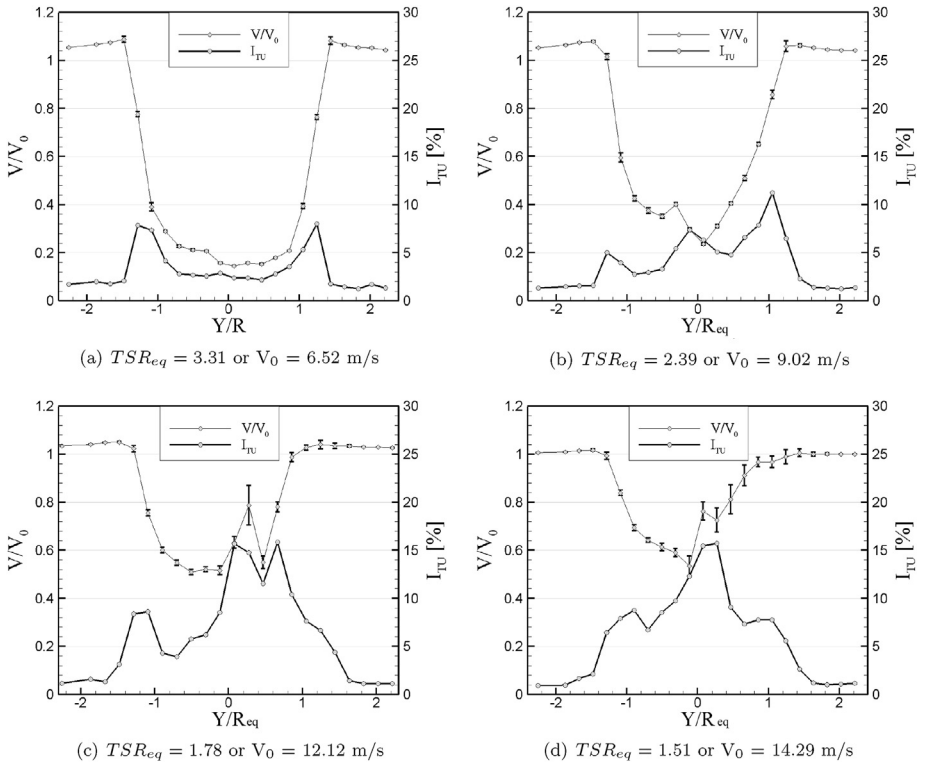
3.2.1. H-shaped turbine

The wake profiles generated by the H-shaped turbine are presented focusing first on the midspan turbine section, considering several operating conditions. The spanwise and streamwise evolution of the wake is then accomplished by means of several different plots for a few relevant spanwise sections along the turbine axis as measured on both the near and the far MSs.

Fig. 13 provides a comprehensive picture of the H-shaped turbine wake at midspan in the near MS, considering four TSR_{eq} conditions including peak C_P ($TSR_{eq} = 2.39$), high load ($TSR_{eq} = 3.31$), low load ($TSR_{eq} = 1.78$) and very low load ($TSR_{eq} = 1.51$) configurations.

First considering the high TSR_{eq} /high-load condition in Fig. 13(a), the wake profile extends beyond the rotor cross section by 40% of the radius on both sides and it features a very high velocity deficit ($V/V_0 = 0.2$) contoured by sharp velocity gradients. Strong shear layers are, therefore, generated between the wake and the freestream flow; as already observed in the wake measurements documented in Ref. [41], the local blockage induced by the wake induces a local over-speed in the freestream flow, which progressively decays far from the wake margin. The measured wake profile is consistent with that presented in Ref. [40] in a measurement position corresponding to the present near traverse (namely, 0.5R away from the cylinder swept by the blades). As expected from the velocity profiles, the shear layers activate relevant turbulent structures, resulting in local peaks of streamwise turbulence intensity.

Even though the wake appears almost symmetric with respect to the turbine axis ($Y/R_{eq} = 0$), the velocity deficit is slightly larger and more uniform on the right side of the wake ($Y/R_{eq} > 0$). The asymmetry with respect to the turbine axis is a typical feature of VAWT wakes, already widely discussed in Ref. [28] on the basis of 2D velocity contours in the wake and also highlighted in Ref. [41], and it is coherent with the working principle of the Darrieus VAWT. Since the tested turbines rotate in counter-clockwise verse, the left side of the wake ($Y/R_{eq} < 0$) is originated by the blade profiles moving windward while the right side of the wake is originated by



(a) $TSR_{eq} = 3.31$ or $V_0 = 6.52$ m/s

(b) $TSR_{eq} = 2.39$ or $V_0 = 9.02$ m/s

(c) $TSR_{eq} = 1.78$ or $V_0 = 12.12$ m/s

(d) $TSR_{eq} = 1.51$ or $V_0 = 14.29$ m/s

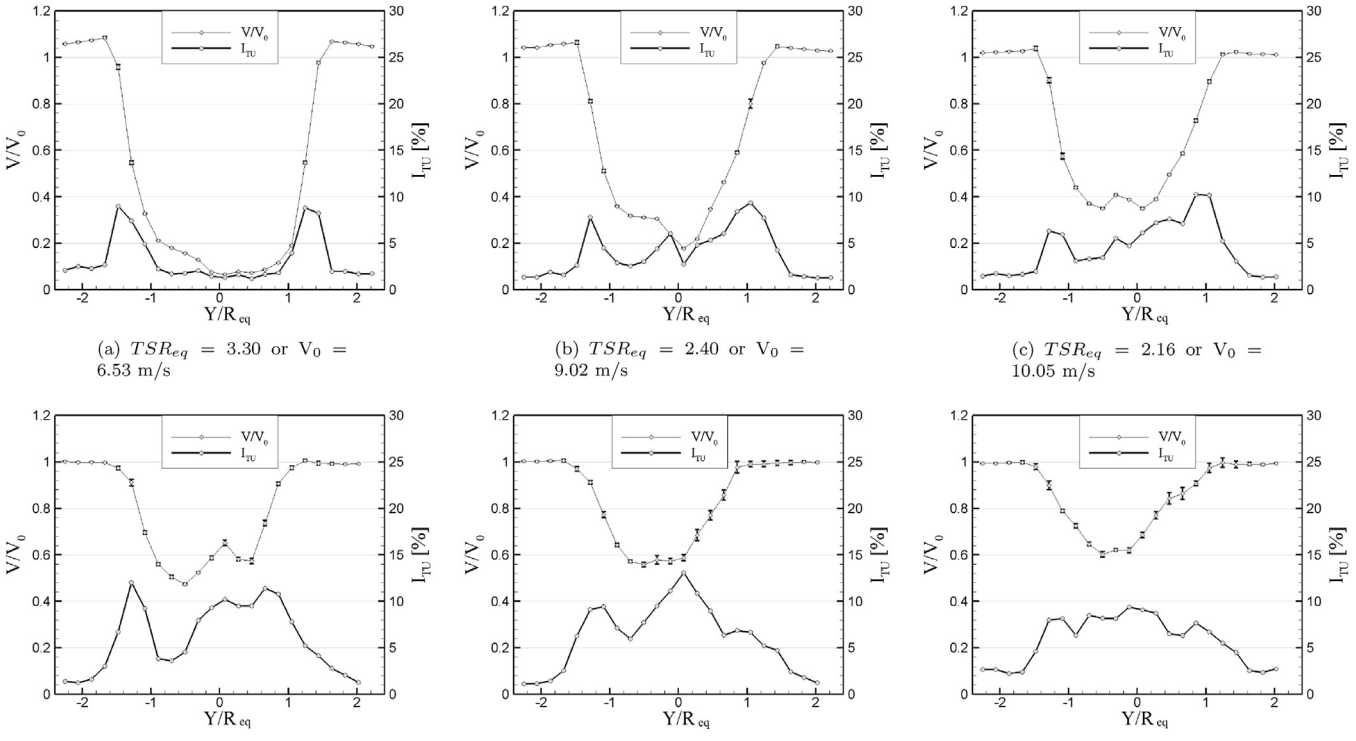
Fig. 13. Velocity and streamwise turbulence intensity profiles at midspan of the H-shaped turbine wake measured in the near MS for four different TSR_{eq} conditions. Intensity of Periodic Unsteadiness is also reported as error bar around the velocity profile. R_{eq} refers to the (constant) radius of the rotor and the transversal coordinate Y is taken null on the rotor axis of rotation.

the blade profiles moving leeward ($Y/R_{eq} > 0$; for a top line drawing of the rotor arrangement, see also Figure 22 in the Appendix). As well known (see, for example, [48]) the composition of velocity triangles is less favorable in the leeward phase, resulting in higher and steeper fluctuations of angle of attack of the flow approaching the blades. For high TSR_{eq} the aerodynamics of the machine are simplified, as the angle of attack tends to remain low during the whole blade rotation, without exceeding the (dynamic) stall limit. For this reason, for sufficiently high TSR_{eq} the distinction between the two sides of the wake tends to reduce [28]. As a further proof of the lower aerodynamic unsteadiness of the blades for high TSR_{eq}, the present measurements show a negligible deterministic unsteadiness in the wake for $TSR_{eq} = 3.31$, suggesting that the wake is statistically stationary at midspan.

A relatively similar configuration is found for peak C_P condition, reported in Fig. 13(b), even though the wake exhibits a lower velocity deficit with respect to the high TSR_{eq} (especially on the windward side, where $V/V_0 = 0.35$). The wake appears clearly asymmetric and slightly displaced towards the windward direction. This is again qualitatively consistent with wake measurements reported in Ref. [41], even though the lower blade number of the present turbine (three against five) reduces the wake deflection, making the measured wake more similar to the one shown in Ref. [40] for a two-blade turbine. The turbulence intensity rises in the whole wake region and especially in the centerline of the wake, marking the trace of the turbine shaft, resulting in a three-peak profile. The deterministic unsteadiness remains very low along both the core and the margin of the wake.

With respect to the wake measurements available in Literature, the present study adds significant information on the wake shed by VAWTs operated at low TSR_{eq} conditions. The reduction of TSR_{eq} below the optimal value has a dramatic impact on the wake, as visible from Fig. 13(c) and (d). The velocity deficit reduces further up to $V/V_0 = 0.5$, and becomes highly oscillating in the right side of the wake ($Y/R_{eq} > 0$), where also the turbulence intensity increases dramatically. In this region, which is originated by the leeward blade motion, the deterministic unsteadiness becomes relevant and quantitatively comparable to the turbulent one, already for $TSR_{eq} = 1.78$. As the TSR_{eq} reduces further to 1.51, the right side of the wake becomes weaker and highly unsteady as a result of the very high oscillations of Reynolds number and angle of attach in the leeward phase of the rotation. These fluctuations are consistent with the periodic detachment of vortices resulting from the onset of dynamic stall in the leeward phase of the blade motion. This is a typical feature of Darrieus VAWTs operating at low loading (see Ref. [49] for a classical flow schematic), and one of the most challenging features to capture by CFD models. The measurements indicate that the traces of dynamic stall start to appear on the near MS for $TSR_{eq} < 2$.

The character of the wakes measured in the near MS is mostly retained in the far MS, as visible from the plots reported in Fig. 14. The velocity profiles are very similar to the ones commented above and appear further shifted on the windward side, as also found by Ref. [40] in a corresponding position (2R away from the cylinder



(a) $TSR_{eq} = 3.30$ or $V_0 = 6.53$ m/s

(b) $TSR_{eq} = 2.40$ or $V_0 = 9.02$ m/s

(c) $TSR_{eq} = 2.16$ or $V_0 = 10.05$ m/s

(d) $TSR_{eq} = 1.80$ or $V_0 = 12.07$ m/s

(e) $TSR_{eq} = 1.51$ or $V_0 = 14.36$ m/s

(f) $TSR_{eq} = 1.33$ or $V_0 = 16.18$ m/s

Fig. 14. Velocity and streamwise turbulence intensity profiles at midspan of the H-shaped turbine wake measured in the far MS for six different TSR_{eq}s. Intensity of Periodic Unsteadiness is also reported as error bar around the velocity profile.

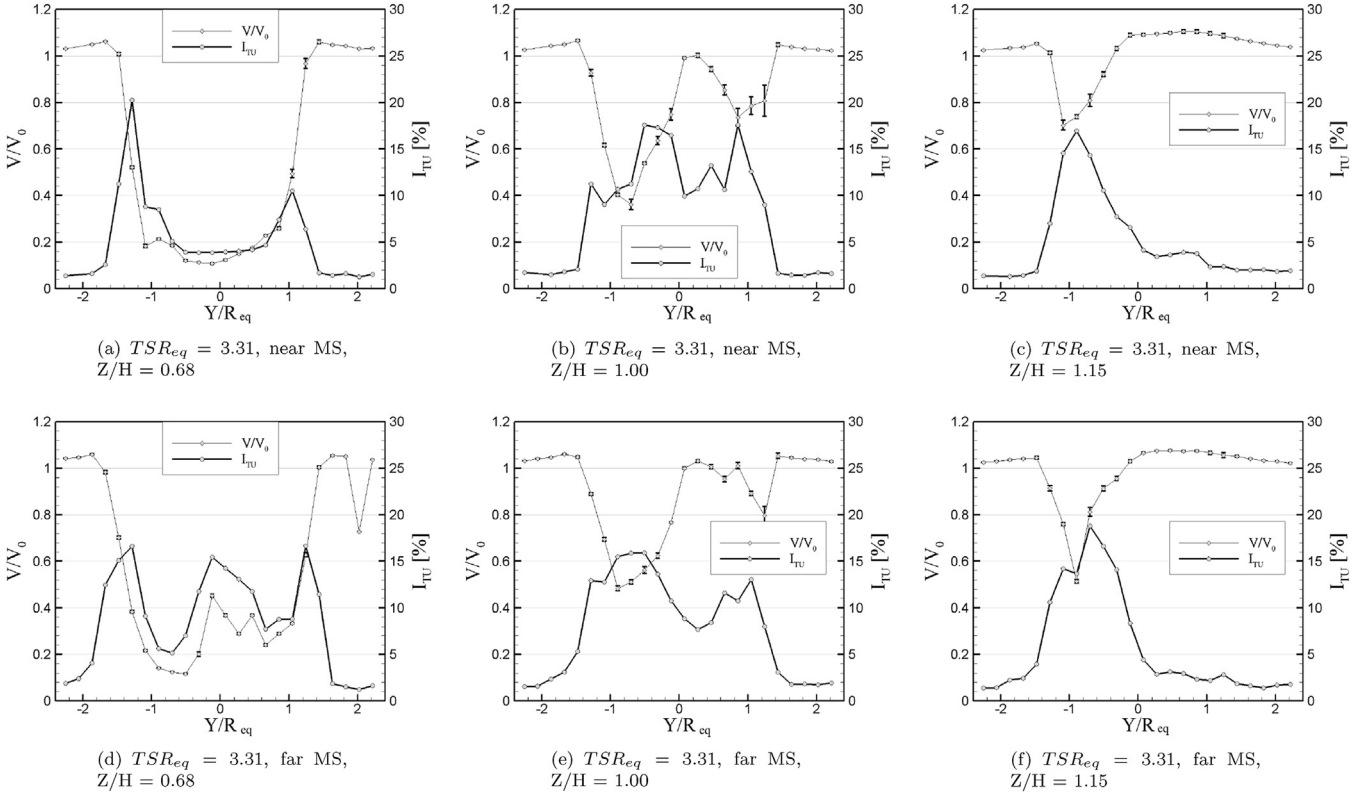
swept by the blades); conversely the turbulence intensity in the core of the wake and the deterministic unsteadiness on the 'leeward' side of the wake result highly weakened even at the lowest TSR_{eq} (equal to 1.33 for the far MS). The mixing process downstream of the turbine has, therefore, smeared the vortexes shed by the dynamic stall, thus smoothing the velocity and turbulence profiles for $TSR_{eq} < 2$. For higher TSR_{eq} conditions, which did not exhibit traces of stall in the measurements on the near MS, the mixing between the two surfaces (that are 1.5 R_{eq} distant each other) does not alter the wake features. It can be concluded that the rate of recovery of the wake is much smaller than the rate of decay of detachment vortexes.

Due to the H-shape of the rotor architecture, the wake features hold for a significant portion of the span, three-dimensional effects being mostly due to the finite length of the blades. The wake measurements performed along the span, summarized in Figs. 15–17 indicate that the tip aerodynamics affect the wake in the top 30% of the half-span of the blade.

For high load conditions ($TSR_{eq} = 3.3$, Fig. 15) the velocity profile measured on the near MS at Z/H = 0.68 (frame a) is very similar to the one at midspan, even though the turbulence intensity rises both in the core of the wake and in the shear layers; the deterministic unsteadiness, instead, remains very low everywhere. In the tip section (frame b) the wake changes dramatically both in term of velocity deficit and unsteadiness; the wake evolves into two separate low-speed/high-turbulence regions on the two sides of the machine, divided by an almost undisturbed zone where the flow velocity recovers the upstream value. Flow angle measurements performed by the present [28] and other [41] authors indicate the onset of large-scale vortices in the tip region of H-shaped VAWTs. In the present case, two counter-rotating vortexes appear on the two sides of the wake at the tip, characterized by a very different magnitude, once again explained by the asymmetry between the windward and leeward phases of the blade operation. The more favorable condition in the windward phase results in a stronger and relatively stable tip vortex on the left side of the wake, while the higher unsteadiness of the leeward phase results in a weaker and highly fluctuating tip vortex on the right side of the wake; this is, therefore, the unique flow structure affected by a relevant deterministic unsteadiness at high load condition. Above the tip section (Z/H = 1.15, frame c) only the tip vortex on the left is sufficiently large to persist and to leave a trace in the wake.

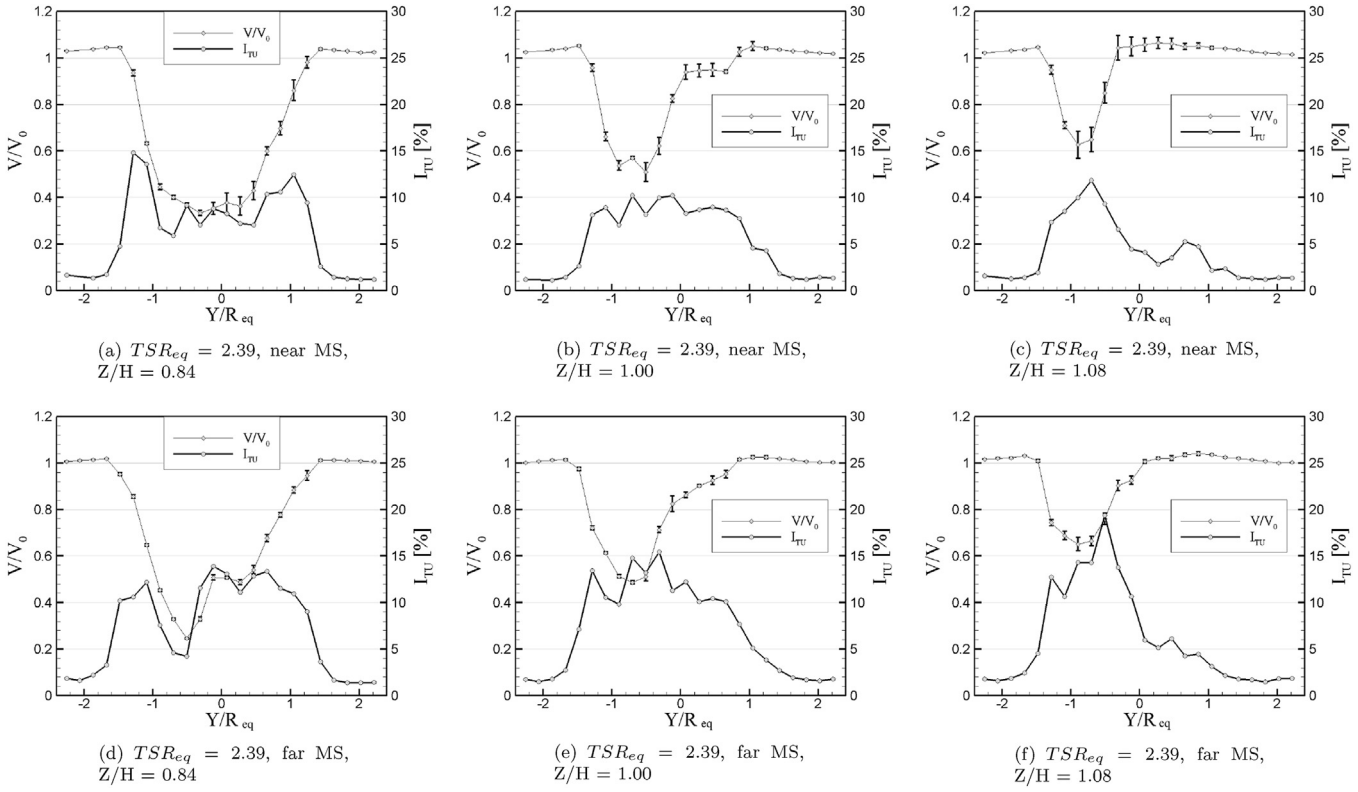
As the wake mixing develops from the near to the far MS (frames d, e, f) the tip vortex structures migrate towards midspan and affect the wake already at Z/H = 0.68, as a double-peak velocity profile and a dramatic increase of turbulence is recorded in this section. As a result, in the tip section the tip vortex on the leeward side appears highly smoothed (and disappears completely above the tip, as already found on the near MS). As also observed at midspan, the mixing process leads to an almost complete decay of any deterministic unsteadiness in the wake.

For maximum C_P condition ($TSR_{eq} = 2.39$, Fig. 16) the spanwise evolution of the wake exhibits a more regular trend, with a progressive reduction of the velocity deficit in the right side of the wake where the deterministic unsteadiness appears also significantly amplified. These are the expected consequences of the amplified fluctuations induced by the reduction of TSR_{eq}, that also results in a severe weakening of the tip vortex on the leeward side, both in terms of velocity deficit and turbulence intensity. It is interesting to note that the deterministic unsteadiness affects most of the wake region even above the tip section. As the wake develops



(a) $TSR_{eq} = 3.31$, near MS, Z/H = 0.68
(b) $TSR_{eq} = 3.31$, near MS, Z/H = 1.00
(c) $TSR_{eq} = 3.31$, near MS, Z/H = 1.15
(d) $TSR_{eq} = 3.31$, far MS, Z/H = 0.68
(e) $TSR_{eq} = 3.31$, far MS, Z/H = 1.00
(f) $TSR_{eq} = 3.31$, far MS, Z/H = 1.15

Fig. 15. Velocity and streamwise turbulence intensity profiles in the tip area of the H-shaped turbine wake measured in the near (top) and far (bottom) MS at $TSR_{eq} = 3.3$ (or $V_0 = 6.5$ m/s). Intensity of Periodic Unsteadiness is also reported as error bar around the velocity profile. H refers to the semi-height of the rotor and the axial, or vertical, coordinate Z is taken positive from the equatorial plane to the tip, so that the equatorial plane corresponds to Z/H = 0.00.



(a) TSR_{eq} = 2.39, near MS, Z/H = 0.84
(b) TSR_{eq} = 2.39, near MS, Z/H = 1.00
(c) TSR_{eq} = 2.39, near MS, Z/H = 1.08
(d) TSR_{eq} = 2.39, far MS, Z/H = 0.84
(e) TSR_{eq} = 2.39, far MS, Z/H = 1.00
(f) TSR_{eq} = 2.39, far MS, Z/H = 1.08

Fig. 16. Velocity and streamwise turbulence intensity profiles in the tip area of the H-shaped turbine wake measured in the near (top) and far (bottom) MS at $TSR_{eq} = 2.39$ (or $V_0 = 9.0$ m/s). Intensity of Periodic Unsteadiness is also reported as error bar around the velocity profile.

downstream these periodic oscillations are smeared and also the velocity profiles start to exhibit the effects of streamwise mixing, as the turbulence intensity increases and the velocity profiles become smoother.

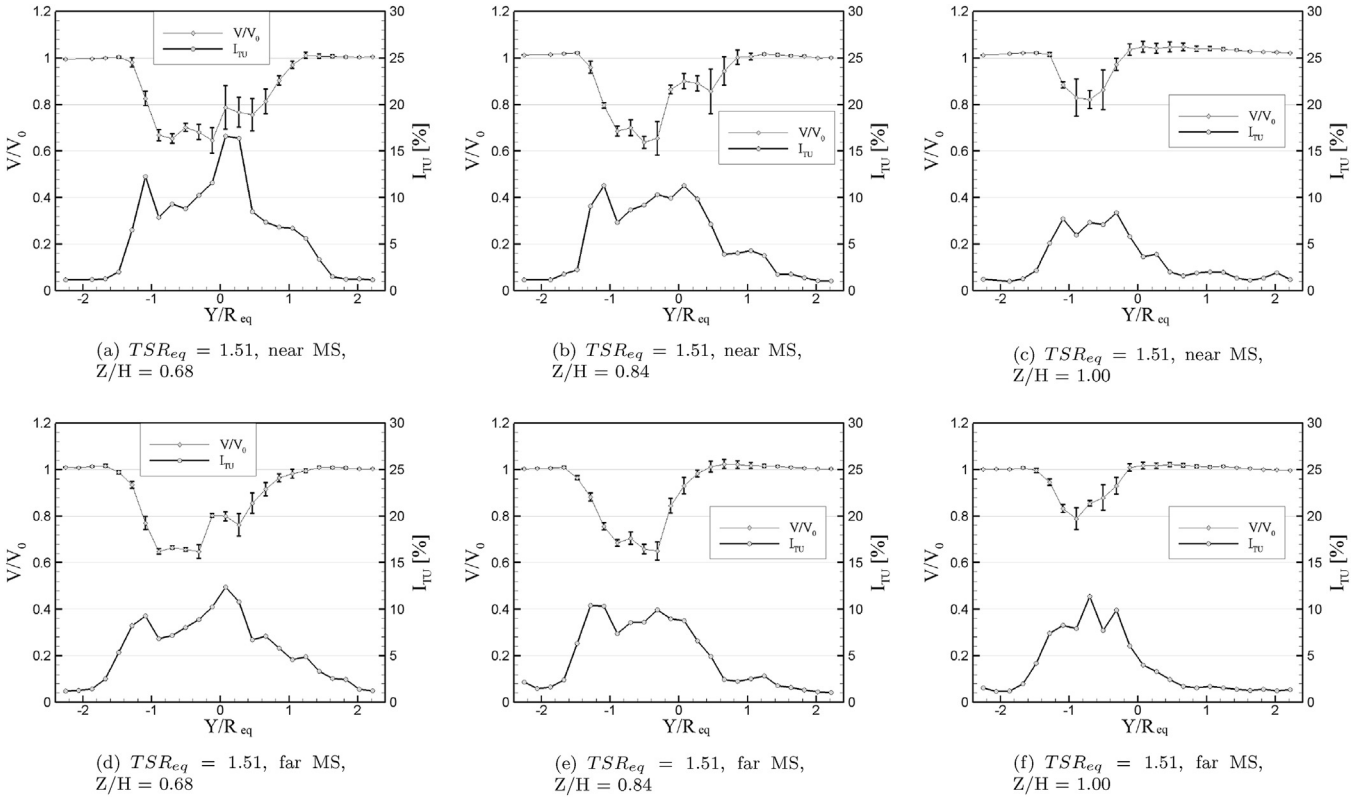
The spanwise and streamwise development of the wake for low loading condition ($TSR_{eq} = 1.5$, Fig. 17) is similar to that observed for maximum C_P, except for the increased amplitude of oscillations. At z/H = 0.68 section for near MS (frame a) a significant deterministic unsteadiness affects the whole wake region, (even though, for obvious reasons, larger oscillations are found in the leeward side of the wake). The wake decays rapidly towards the tip, and the velocity recovers the upstream value in the sections just above the tip (not reported, for this reason, in the Figure). In the tip section (frame c) only a small trace of the wake appears on the left side of the rotor, and it is affected by large deterministic oscillations whose amplitude reaches 100% of the local velocity defect. These features suggest that, for sufficiently low TSR_{eq}, the blade tip aerodynamics becomes highly unsteady also in the windward phase of rotation, resulting in a weakened tip vortex. As the wake develops downstream (frames d, e, f) the velocity and turbulence profiles are smoothed and the amplitude of the deterministic unsteadiness reduces, even though remaining significant, especially in the tip section. The pulsating tip vortex appears to be a persistent structure in the flow downstream of the tested H-shaped VAWT.

3.2.2. Troposkien turbine

As done for the H-shaped machine, the troposkien turbine wake is studied focusing first on the midspan (or equatorial) section, and then analyzing its spanwise and streamwise development.

Fig. 18 reports the distribution of velocity, turbulence and deterministic unsteadiness measured at midspan for four TSR_{eq} conditions including high load ($TSR_{eq} = 4.04$), max C_P ($TSR_{eq} = 3.11$), low load ($TSR_{eq} = 2.40$) and very low load ($TSR_{eq} = 1.80$) configurations. As the flat and curved MSs coincide at midspan, the equatorial wake measurements are available at a single distance from the rotor. The symmetric and lowly tapered shape of the troposkien curve around the equatorial zone inhibits the onset of 3D effects in rotor aerodynamics at midspan. As a result, the equatorial wake profiles for the troposkien turbine strictly resemble the ones observed for the H-shaped turbine (provided that the TSR_{eq} is augmented by approximatively 0.7). As the TSR_{eq} reduces from 4 to 2.4, the wake evolves from a large and nearly uniform zone of velocity deficit in a highly asymmetric structure featuring lower velocity deficit, higher turbulence and higher deterministic unsteadiness in the right side of the wake. This is due to the larger and steeper fluctuations of incidence and Reynolds number experienced by the blades during the leeward motion. In fact, the lowest TSR_{eq} (1.8) condition exhibits a fairly different wake configuration, featuring a very small wake deficit and comparable unsteadiness on the two sides of the wake, not observed for the H-shaped turbine (which was tested up to $TSR_{eq} = 1.33$, probably not low enough for finding a corresponding condition to the troposkien turbine operated at $TSR_{eq} = 1.8$). The differences between the two machines can be, at least partially, explained considering the larger Reynolds number established in the equatorial section of the troposkien turbine, which has a greater diameter with respect to the H-shaped machine.

The highly tapered shape of the troposkien configuration away from midspan induces a dramatic spanwise evolution of the wake profiles. Figs. 19–21 report about the wake measured on three relevant spanwise sections, the first one at (about) midway between the equatorial plane and the tip (Z/H = 0.43), the second one



(a) TSR_{eq} = 1.51, near MS, Z/H = 0.68

(b) TSR_{eq} = 1.51, near MS, Z/H = 0.84

(c) TSR_{eq} = 1.51, near MS, Z/H = 1.00

(d) TSR_{eq} = 1.51, far MS, Z/H = 0.68

(e) TSR_{eq} = 1.51, far MS, Z/H = 0.84

(f) TSR_{eq} = 1.51, far MS, Z/H = 1.00

Fig. 17. Velocity and streamwise turbulence intensity profiles in the tip area of the H-shaped turbine wake measured in the near (top) and far (bottom) MS at $TSR_{eq} = 1.5$ (or $V_0 = 14.3$ m/s). Intensity of Periodic Unsteadiness is also reported as error bar around the velocity profile.

closer to the tip (Z/H = 0.14) and the third one exactly at the tip (Z/H = 0.0).

For high load condition, only investigated on the curved MS, the intermediate section (frame a of Fig. 19) shows a smaller wake region, although the velocity defect and the turbulence intensity remain close to the midspan values. A net increase of deterministic unsteadiness is detected in the shear layers, resulting from the reduction of the local tip speed ratio caused by the reduction of diameter. These features are strongly amplified at Z/H = 0.14 (frame b), where a narrow and highly unsteady wake is measured. The wake reduces further in the tip section, where a significant increase of turbulence is measured, with peak values in the shear layer on the right side of the wake. These charts indicate that flow detachment is activated in a small region of the troposkien turbine even at high load condition, inducing unsteady flows in local regions of the wake. Unsteady effects appear at high load also for the H-shaped machine in the tip region, but they are connected to the periodic variation of a large-scale tip vortex. For the troposkien turbine, instead, the region affected by wide oscillations involves a small amount of the flow rate passing through the rotor, reducing the impact of the flow unsteadiness on the overall rotor aerodynamics.

In Fig. 20 the wake profiles measured for optimal C_P conditions are shown on the three relevant sections for both the curved and flat MSs. The spanwise evolution of the wake on the curved MS (top frames) resembles the one observed for $TSR_{eq} = 4$, even though larger deterministic unsteadiness is detected in the sections close to the tip. The streamwise evolution of the wake from the curved to the flat surfaces indicates that the velocity and turbulence profiles at the intermediate section (frame a and d) are almost unaffected by the mixing despite the streamwise distance between the two MSs, at this section, amounts to 0.3 R_{eq}. Conversely, a significant streamwise mixing occurs in the tip section (frames c and f), where the velocity profile reveals an enlarged and smoothed wake on the left side, and the turbulence intensity reduces. The deterministic unsteadiness also reduces in the flat MS, but mostly on the right side of the wake; this suggests that the viscous structures periodically shed by the blade during the leeward motion experience a higher decay rate than the corresponding ones on the windward phase, resulting in a similar unsteadiness on the two sides of the wake sufficiently far from the rotor.

Finally, considering the low loading condition for $TSR_{eq} = 2.40$, reported in Fig. 21 for the three spanwise sections on the curved MS, it is worth noting that the wake profile in the intermediate section resembles the one in the equatorial section; in particular a very limited unsteadiness is measured, even though the local TSR_{eq} in this section amounts to approximatively 1.65. Extremely large unsteady fluctuations are instead found in the tip region, where the deterministic oscillations become comparable with the velocity defect. As expected, the deterministic unsteadiness is by far higher on the right side of the wake.

The character of the wake unsteadiness, the wake development in spanwise and streamwise direction, as well as the wake evolution with the operating condition clarify the complexity of the VAWT aerodynamics, and provide a justification for the difficulties that computational techniques have to face in VAWT performance prediction and aerodynamic design.

4. Conclusions

This paper has critically revised the main extensive wind tunnel campaigns conducted on VAWTs in the last 15 years,

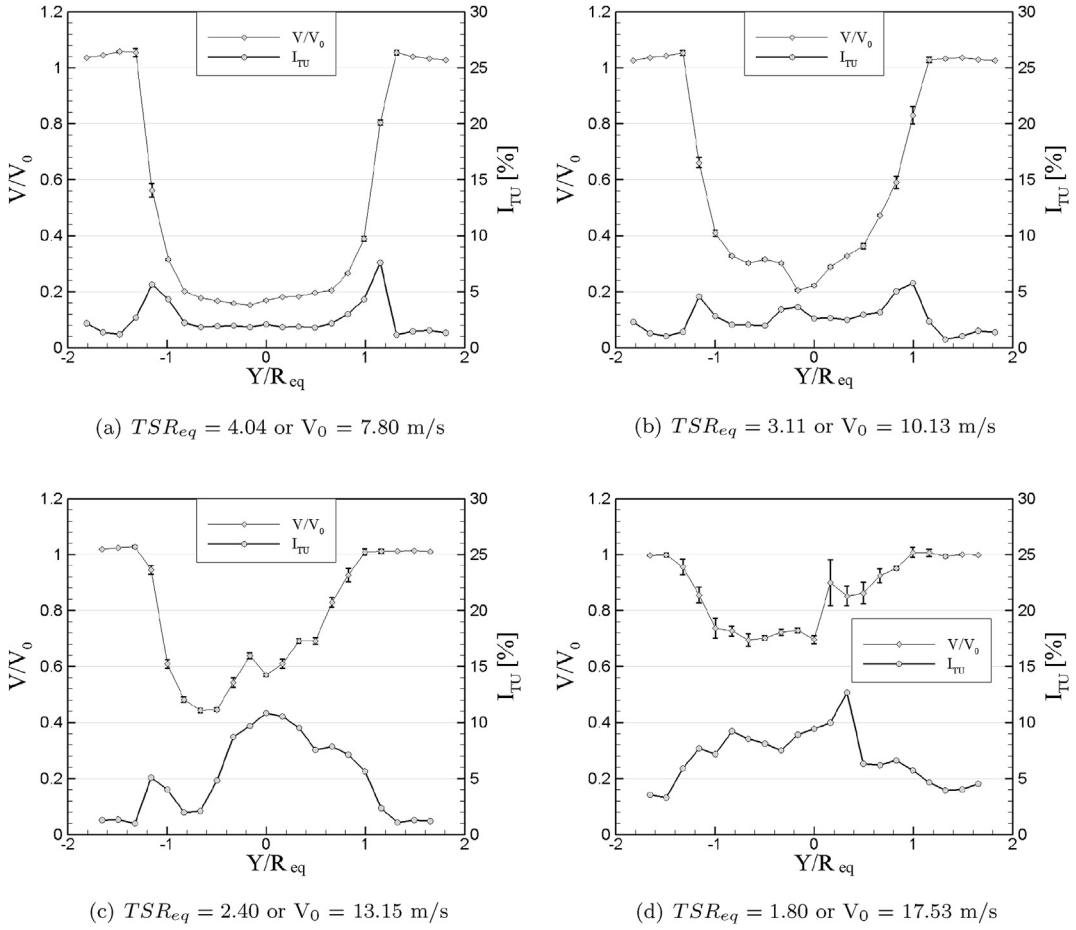


Fig. 18. Velocity and streamwise turbulence intensity profiles in the equatorial section of the troposkien turbine wake for four different TSR_{eq} conditions. Intensity of Periodic Unsteadiness is also reported as error bar around the velocity profile. The transversal coordinate Y is taken null on the rotor axis of rotation.

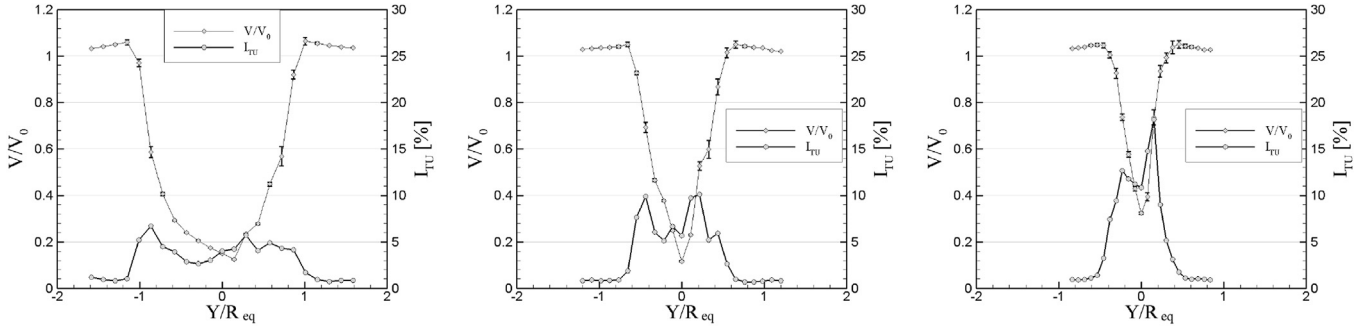
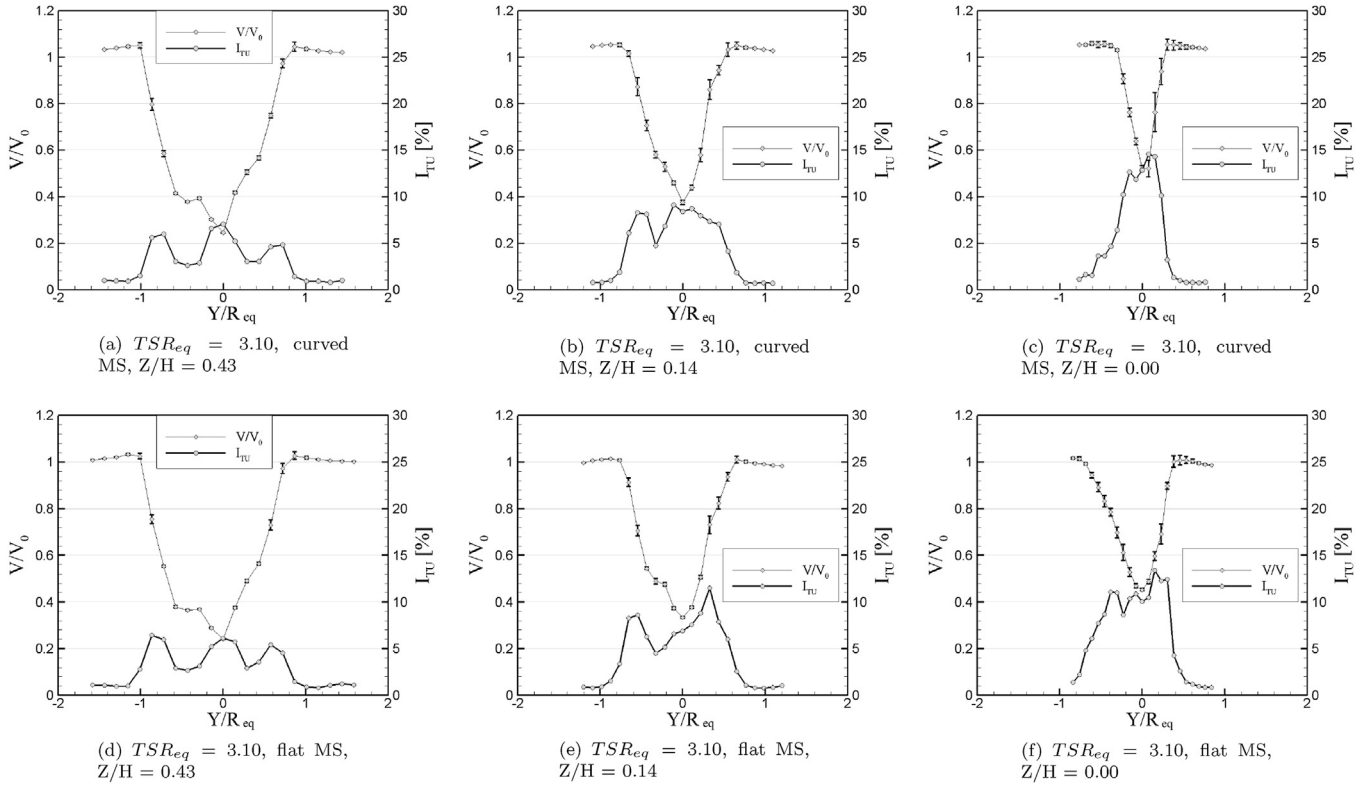


Fig. 19. Velocity and streamwise turbulence intensity profiles for different axial sections of the troposkien turbine wake for $TSR_{eq} = 4.04$ on the curved MS. Intensity of Periodic Unsteadiness is also reported as error bar around the velocity profile. H refers to the semi-height of the rotor and the axial, or vertical, coordinate Z is taken positive from tip to the equatorial plane, so that the equatorial plane corresponds to Z/H = 1.00.

highlighting some important weaknesses occurring during the measurement process, such as: a too high blockage ratio, a too low blade Reynolds number and a general lack of information about some important aspects of the flow field (such as the definition of the turbulence intensity of the incoming wind) and rotor geometry (such as the geometry of the spokes and their position with respect to the blade profiles). Aiming at filling such gap, the results of an experimental campaign conducted in controlled flow conditions (i.e. low turbulence wind tunnel) on two different rotor architectures (H-shaped and troposkien) of equal swept area have been presented with a two-fold objective: providing a fully detailed benchmark for three-dimensional



(a) TSR_{eq} = 3.10, curved MS, Z/H = 0.43 (b) TSR_{eq} = 3.10, curved MS, Z/H = 0.14 (c) TSR_{eq} = 3.10, curved MS, Z/H = 0.00

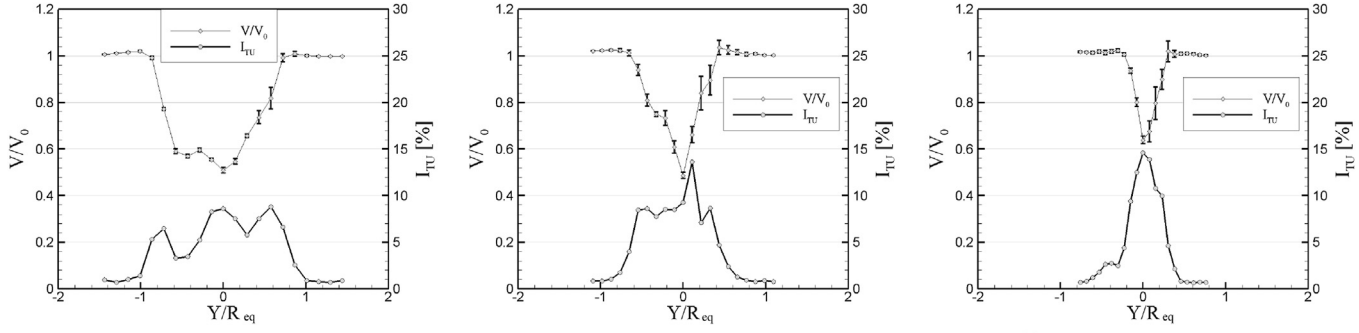
(d) TSR_{eq} = 3.10, flat MS, Z/H = 0.43 (e) TSR_{eq} = 3.10, flat MS, Z/H = 0.14 (f) TSR_{eq} = 3.10, flat MS, Z/H = 0.00

Fig. 20. Velocity and streamwise turbulence intensity profiles for different axial sections of the troposkien turbine wake for TSR_{eq} = 3.10 on the curved (top) and flat (bottom) MS. Intensity of Periodic Unsteadiness is also reported as error bar around the velocity profile.

VAWT numerical simulations and investigating the difference between such two well-known VAWT architectures in terms of aerodynamic performance and thrust, as well as wake characteristics.

Typical stall power curves were obtained for both rotors. Interestingly, a self-limitation of the power delivered by the troposkien rotor was observed at high wind speeds, where it flattens at 70% of the peak power. A marked increase in the power extraction of the troposkien configuration was clearly registered, suggesting that the reduction of both blade tip losses and parasitic drag (due to the absence of the spokes) have a beneficial effect on the overall aerodynamic performance of small scale rotors, if compared to the H-shape configuration. Nevertheless, the measured higher aerodynamic efficiency of the troposkien rotor could also be promoted by a higher equatorial blade Reynolds number (due to the resulting larger equatorial radius with respect to the one of the H-shaped architecture). On the other hand, quite similar thrust values were experienced by the two tested rotors, suggesting that the same rotor swept area, blade section and rotational speed drive to similar aerodynamic thrusts, despite the different power exchange.

Flow measurements downstream of the rotor for several streamwise and spanwise positions have shown the fully three-dimensional and unsteady character of VAWT wakes. The turbine working condition has a dramatic impact on the wake features, which appears almost unaffected by the periodic unsteadiness at high tip speed ratios. On the contrary, at low tip speed ratios the wake appears less symmetric, reduced in extension and velocity defect, and affected by much wider areas of high turbulent and periodic unsteadiness. The work exchange process and, as a



(a) TSR_{eq} = 2.40, curved MS, Z/H = 0.43 (b) TSR_{eq} = 2.40, curved MS, Z/H = 0.14 (c) TSR_{eq} = 2.40, curved MS, Z/H = 0.00

Fig. 21. Velocity and streamwise turbulence intensity profiles for different axial sections of the troposkien turbine wake for TSR_{eq} = 2.40 on the curved MS. Intensity of Periodic Unsteadiness is also reported as error bar around the velocity profile.

consequence, the main wake features and evolution have also been found strongly affected by the rotor architecture. A comparison analysis reveals that the blades of both the tested turbines are interested by severe dynamic-stall phenomena at low tip-speed-ratio. However, the tapered shape of the troposkien architecture seems to mitigate the effects of stall, mostly occurring in the tip region, where relatively small vortices are generated, being rapidly mixed-out just downstream of the turbine. Conversely, the tip region of the H-shaped rotor wake is affected by a large and persistent tip vortex.

Besides the here presented initial findings, where the attention was paid on the time-mean characteristics of rotors performance and of their wake, the present experimental data-base allows to carry out a deeper investigation on the unsteady evolution of the flow features (in terms of rotor power and thrust as well as of wake meandering downstream of the test section) that might be performed by resorting to an integrated experimental and CFD campaign, aiming at further exploring the difference between the two tested rotor architectures.

Finally, the data gathered have been listed and formatted to serve as to experimental benchmark, to complement and support validation and calibration of numerical codes.

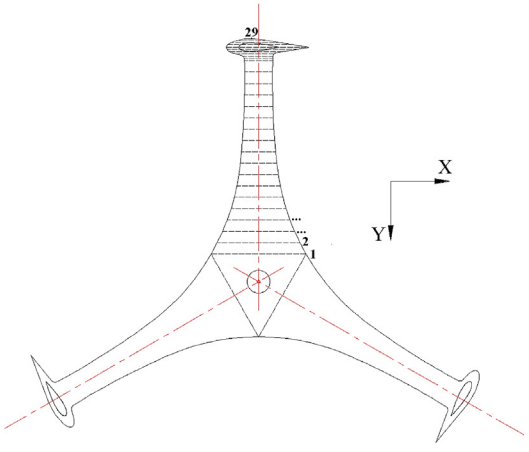
Acknowledgements

The authors would like to thanks the MIUR (Italian Ministry of Education, University and Research) for funding the research project, the DeepWind project of the European Union's Seventh Framework Programme (FP7/2007–2013) for funding the troposkien VAWT, the Company Tozzi-Nord Wind Turbines for providing the H-shaped VAWT, as well as the technicians and collaborators of both University of Trento and Politecnico di Milano for their precious support before and during the tests.

Nomenclature

A_s	rotor swept area [m^2]
C_X	rotor longitudinal thrust coefficient [−]
C_Y	rotor transversal thrust coefficient [−]
$C_{P,aero}$	aerodynamic power coefficient [−]
c	chord length [m]
H	rotor semi-height [m]
H_{wt}	wind tunnel height [m]
h	local rotor height [m]
I	flow turbulence [−]
L	blade length [m]
Q_{aero}	aerodynamic torque [Nm]
P_{aero}	aerodynamic power [W]
Re^+	maximum blade Reynolds number $= (\Omega R_{eq} + V_0)\, c/\nu$ [−]
Re^-	minimum blade Reynolds number $= (\Omega R_{eq} - V_0)\, c/\nu$ [−]
Re_c	chord Reynolds number $= \Omega R_{eq}\, c/\nu$ [−]
R_{eq}	maximum rotor radius [m]
r	local rotor radius [m]
TSR_{eq}	equatorial tip speed ratio [−]
T_X	rotor longitudinal thrust [N]
T_Y	rotor transversal thrust [N]
t	blade thickness [m]
u_{Qaero}	aerodynamic torque uncertainties [Nm]
u_{TX}	longitudinal thrust uncertainties [N]
u_{TY}	transversal thrust uncertainties [N]
u_V	velocity uncertainties [°C]
u_Θ	temperature uncertainties [°C]
u_ρ	density uncertainties [kg/m^3]
$u_{\Omega m}$	angular velocity uncertainties [rpm]
V_0	free stream velocity [m/s]
W_{wt}	wind tunnel width [m]
ε	3D geometric blockage [%]
Θ	free stream temperature [°C]
ν	free stream kinematic viscosity [m^2/s]
Ω	rotor angular velocity [rpm]
Ω_m	measured rotor angular velocity [rpm]
Ω_n	nominal rotor angular velocity [rpm]
ρ	free stream density [kg/m^3]

Appendix



Sec. No.	*X* [*mm*]	*Y* [*mm*]	*Sec. No.*	*X* [*mm*]	*Y* [*mm*]
1	104.8	-60.5	16	30.5	-435.5
	-104.8	-60.5		-30.5	-435.5
2	91.6	-85.5	17	30.5	-460.5
	-91.6	-85.5		-30.5	-460.5
3	79.4	-110.5	18	31.1	-485.5
	-79.4	-110.5		-31.1	-485.5
4	69.0	-135.5	19	83.5	-510.5
	-69.0	-135.5		-69.4	-510.5
5	60.4	-160.5	20	31.3	-490.5
	-60.4	-160.5		-31.6	-490.5
6	53.4	-185.5	21	31.6	-495.5
	-53.4	-185.5		-34.8	-495.5
7	47.8	-210.5	22	34.3	-500.5
	-47.8	-210.5		-51.9	-500.5
8	43.5	-235.5	23	53.0	-505.5
	-43.5	-235.5		-63.7	-505.5
9	40.3	-260.5	24	104.8	-515.5
	-40.3	-260.5		-70.9	-515.5
10	37.8	-285.5	25	76.6	-520.5
	-37.8	-285.5		-68.6	-520.5
11	35.7	-310.5	26	46.4	-525.5
	-35.7	-310.5		-61.9	-525.5
12	33.8	-335.5	27	16.2	-530.5
	-33.8	-335.5		-48.2	-530.5
13	32.3	-360.5	28	0.3	-533.0
	-32.3	-360.5		-34.4	-533.0
14	31.5	-385.5	29	-16.0	-534.0
	-31.5	-385.5			
15	30.9	-410.5			
	-30.9	-410.5			

Fig. 22. Drawing of the spokes connecting H-shaped rotor blades to the central shaft: the reference sections (corresponding to dashed lines numbered from 1 to 29, starting from inward to outward) of the first spoke are also represented; the origin of the Cartesian axes is located at the axis of revolution.

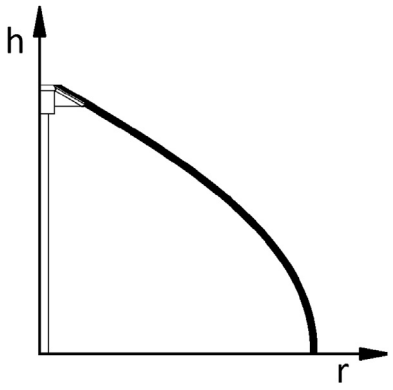


Fig. 23. Cylindrical coordinates (r, h) of the troposkien blade longitudinal axis. This blade axis is placed in c/2 along the chord line and in half thickness of the blade. Moreover, it is always orthogonal to the airfoil plane.

Table 7
Cylindrical coordinates (r, h) of the troposkien blade longitudinal axis.

Station[−]	*r* [mm]	*h* [mm]	*Station*[−]	*r* [mm]	*h* [mm]	*Station*[−]	*r* [mm]	*h* [mm]	*Station*[−]	*r* [mm]	*h* [mm]
1	0	755.0	26	188.7	644.6	51	377.5	523.6	76	566.2	371.7
2	7.5	750.6	27	196.3	640.0	52	385.0	518.3	77	573.8	364.3
3	15.1	746.3	28	203.8	635.5	53	392.6	513.0	78	581.3	356.8
4	22.6	741.9	29	211.4	630.9	54	400.1	507.7	79	588.9	349.1
5	30.2	737.6	30	218.9	626.3	55	407.7	502.2	80	596.4	341.2
6	37.7	733.2	31	226.5	621.7	56	415.2	496.8	81	604.0	333.1
7	45.3	728.9	32	234.0	617.0	57	422.8	491.2	82	611.5	324.8
8	52.8	724.5	33	241.6	612.4	58	430.3	485.7	83	619.1	316.3
9	60.4	720.1	34	249.1	607.7	59	437.9	480.0	84	626.6	307.6
10	67.9	715.7	35	256.7	603.0	60	445.4	474.3	85	634.2	298.5
11	75.5	711.4	36	264.2	598.2	61	453.0	468.5	86	641.7	289.2
12	83.0	707.0	37	271.8	593.5	62	460.5	462.7	87	649.3	279.5
13	90.6	702.6	38	279.3	588.7	63	468.1	456.8	88	656.8	269.5
14	98.1	698.2	39	286.9	583.9	64	475.6	450.8	89	664.4	259.1
15	105.7	693.8	40	294.4	579.0	65	483.2	444.8	90	671.9	248.2
16	113.2	689.4	41	302.0	574.2	66	490.7	438.6	91	679.5	236.8
17	120.8	684.9	42	309.5	569.3	67	498.3	432.4	92	687.0	224.8
18	128.3	680.5	43	317.1	564.3	68	505.8	426.1	93	694.6	212.1
19	135.9	676.1	44	324.6	559.4	69	513.4	419.7	94	702.1	198.5
20	143.4	671.6	45	332.2	554.4	70	520.9	413.2	95	709.7	183.9
21	151.0	667.1	46	339.7	549.4	71	528.5	406.6	96	717.2	168.0
22	158.5	662.7	47	347.3	544.3	72	536.0	399.8	97	724.8	150.4
23	166.1	658.2	48	354.8	539.2	73	543.6	393.0	98	732.3	130.3
24	173.6	653.7	49	362.4	534.0	74	551.1	386.0	99	739.9	10.7
25	181.2	649.1	50	369.9	528.8	75	558.7	378.9	100	747.4	7.5
									101	755.0	0

Table 8
Measured data for the H-shaped rotor.

V_0 [m/s]	$u_{V_0[95\%]}$ [m/s]	T [°C]	$u_{T[95\%]}$ [°C]	ρ [kg/m^3]	$u_{\rho[95\%]}$ [kg/m^3]	Ω_n [rpm]	Ω_m [rpm]	$u_{\Omega_m[95\%]}$ [rpm]	Q_{aero} [Nm]	$u_{Q[95\%]}$ [Nm]	T_X[N]	$u_{T_X[95\%]}$ [N]	T_Y[N]	$u_{T_Y[95\%]}$ [N]	Re^+[−]	Re^-[−]
6.09	0.12	24.95	0.12	1.160	0.0018	400	398.47	0.05	0.35	0.19	26.82	0.94	2.63	0.59	1.5E+05	8.3E+04
6.53	0.12	25.90	0.12	1.155	0.0018	400	400.21	0.05	0.89	0.19	31.43	0.97	3.08	0.59	1.5E+05	8.1E+04
7.99	0.12	25.03	0.12	1.157	0.0018	400	400.31	0.06	3.01	0.19	47.95	1.14	6.40	0.61	1.6E+05	7.4E+04
9.02	0.12	25.76	0.12	1.155	0.0018	400	400.97	0.05	4.21	0.19	58.41	1.25	7.30	0.62	1.7E+05	6.8E+04
10.01	0.12	25.03	0.12	1.157	0.0018	400	401.09	0.06	4.56	0.19	66.02	1.34	7.83	0.62	1.7E+05	6.3E+04
12.00	0.12	25.03	0.12	1.154	0.0018	400	400.75	0.05	3.93	0.19	78.64	1.48	15.02	0.67	1.8E+05	5.2E+04
14.13	0.12	25.03	0.12	1.154	0.0018	400	400.52	0.05	3.49	0.19	94.37	1.66	23.02	0.74	1.9E+05	4.0E+04
14.36	0.12	26.90	0.12	1.153	0.0018	400	401.20	0.05	3.51	0.19	96.01	1.67	23.91	0.74	1.9E+05	3.9E+04
16.18	0.12	25.03	0.12	1.153	0.0018	400	400.08	0.09	2.94	0.19	112.61	1.87	34.37	0.84	2.0E+05	2.9E+04

Table 9
Measured data for the troposkien rotor.

V_0 [m/s]	$u_{V_0[95\%]}$ [m/s]	T [°C]	$u_{T[95\%]}$ [°C]	ρ [kg/m^3]	$u_{\rho[95\%]}$ [kg/m^3]	Ω_n [rpm]	Ω_m [rpm]	$u_{\Omega_m[95\%]}$ [rpm]	Q_{aero} [Nm]	$u_{Q[95\%]}$ [Nm]	T_X[N]	$u_{T_X[95\%]}$ [N]	T_Y[N]	$u_{T_Y[95\%]}$ [N]	$Re^+[-]$	$Re^-[-]$
3.15	0.12	23.6	0.12	1.171	0.0018	400	398.80	0.05	−1.56	0.18	5.99	0.56	−1.19	1.14	1.9E+05	1.5E+05
4.15	0.12	22.6	0.12	1.175	0.0018	400	398.92	0.13	−1.37	0.18	9.21	0.61	−1.19	1.13	1.9E+05	1.5E+05
5.13	0.12	22.13	0.12	1.177	0.0018	400	399.09	0.08	−0.95	0.18	14.48	0.60	0.09	1.13	2.0E+05	1.4E+05
6.2	0.12	21.6	0.12	1.179	0.0018	400	399.56	0.08	−0.15	0.18	22.85	0.65	1.74	1.13	2.0E+05	1.4E+05
7.3	0.12	22.2	0.12	1.177	0.0018	400	399.94	0.07	1.46	0.18	34.16	0.79	−0.38	1.13	2.1E+05	1.3E+05
7.31	0.14	22.2	0.12	1.177	0.0018	400	399.91	0.05	1.42	0.18	33.69	0.72	−0.23	1.13	2.1E+05	1.3E+05
8.2	0.12	21.16	0.12	1.180	0.0018	400	400.95	0.06	3.21	0.18	43.80	0.79	−1.65	1.13	2.2E+05	1.3E+05
9.19	0.12	20.7	0.12	1.183	0.0018	400	401.22	0.06	5.42	0.18	56.34	0.86	−2.57	1.13	2.2E+05	1.2E+05
9.61	0.12	20.8	0.12	1.179	0.0018	400	401.20	0.05	6.38	0.19	63.07	0.91	−1.57	1.13	2.2E+05	1.2E+05
10.17	0.12	21	0.12	1.180	0.0018	400	401.11	0.05	7.70	0.19	67.62	0.94	−2.92	1.13	2.3E+05	1.2E+05
10.48	0.12	20.5	0.12	1.184	0.0018	400	401.04	0.05	8.38	0.19	71.78	0.96	−2.30	1.14	2.3E+05	1.1E+05
11.08	0.12	20.7	0.12	1.182	0.0018	400	400.89	0.06	9.58	0.20	75.85	1.16	−3.84	1.14	2.3E+05	1.1E+05
12.12	0.12	20.7	0.12	1.183	0.0018	400	400.77	0.06	10.44	0.18	83.51	1.05	−5.84	1.13	2.4E+05	1.1E+05
13.33	0.12	20.7	0.12	1.183	0.0018	400	400.85	0.07	9.54	0.19	89.96	1.14	−10.94	1.15	2.4E+05	9.9E+04
14.21	0.12	20.8	0.12	1.180	0.0018	400	400.86	0.09	9.39	0.18	95.90	1.14	−13.84	1.14	2.5E+05	9.5E+04
15.15	0.12	20.7	0.12	1.183	0.0018	400	401.03	0.42	8.78	0.25	103.07	1.23	−19.26	1.38	2.5E+05	9.0E+04
15.97	0.12	20.7	0.12	1.183	0.0018	400	401.04	0.08	7.92	0.18	108.62	1.21	−24.52	1.14	2.6E+05	8.5E+04
17.02	0.14	20.7	0.12	1.180	0.0018	400	401.09	0.49	7.78	0.18	115.10	3.23	−27.80	1.84	2.6E+05	7.9E+04
17.93	0.12	20.7	0.12	1.180	0.0018	400	401.06	0.06	7.76	0.18	121.48	1.30	−30.02	1.14	2.7E+05	7.5E+04
18.96	0.12	20.7	0.12	1.180	0.0018	400	400.99	0.13	7.80	0.19	130.16	1.37	−32.79	1.15	2.7E+05	6.9E+04
20.01	0.12	20.7	0.12	1.180	0.0018	400	401.02	0.06	7.86	0.18	139.72	1.44	−36.36	1.16	2.8E+05	6.3E+04

References

[1] H. Glauert, Airplane propellers, aerodynamic theory, Public. Inc. 4 (L) (1963) 169–360.
[2] J. Strickland, The Darrieus Turbine: a Performance Prediction Model Using Multiple Streamtube, SAND75–0431.
[3] I. Paraschivoiu, Double-multiple Streamtube Model for Darrieus Wind Turbines, NASA Conference Publication 2185.
[4] I. Paraschivoiu, F. Delclaux, Double multiple streamtube model with recent improvements, J. Energy 7 (1983) 250–255.
[5] J. Strickland, T.W. Nguyen, A vortex model of the darrieus turbine: an analytical and experimental study, J. Fluid Eng. 101 (1979) 50–505.
[6] F. Bassi, A. Ghidoni, A.P.S. Rebay, A. Crivellini, N. Franchina, M. Savini, A high-order discontinuous galerkin solver for the incompressible rans and $k-\omega$ turbulence model equations, Comput. Fluids 98 (2014) 54–68.
[7] S. Shamsoddin, F. Porté-Agel, Large eddy simulation of vertical axis wind turbine wakes, Energies 7 (2014) 890–912.
[8] F. Trivellato, M. Raciti Castelli, On the courant-friedrichs-lewy criterion of rotating grids in 2d vertical-axis wind turbine analysis, Renew. Energy 62 (2014) 53–62.
[9] A. Balduzzi, A. Bianchini, F. Gigante, G. Ferrara, M. Campobasso, L. Ferrari, Parametric and comparative assessment of Navier-Stokes cfd methodologies for darrieus wind turbine performance analysis, Proceedings of the ASME Turbo Expo 2015Paper GT2015-42663.
[10] H.F. Lam, H.Y. Peng, Study of wake characteristics of a vertical axis wind turbine by two-and three-dimensional computational uid dynamics simulations, Renew. Energy 90 (2016) 386–398.
[11] M. Abkar, J.O. Dabiri, Self-similarity and ow characteristics of vertical-axis wind turbine wakes: an les study, J. Turbul. 18 (2017) 373–389.
[12] A. Bianchini, A. Balduzzi, G. Ferrara, L. Ferrari, G. Persico, V. Dossena, L. Battisti, Detailed analysis of the wake structure of a straight-blade H-Darrieus wind turbine by means of wind tunnel experiments and CFD simulations, J. Eng. Gas Turbines Power 140, paper 032604.
[13] C. Bottasso, F. Campagnolo, V. Petrovic, Wind tunnel testing of scaled wind turbine models: beyond aerodynamics, J. Wind Eng. Ind. Aerod. 127 (2014) 11–28.
[14] R. Howell, N. Qin, J. Edwards, N. Durrani, Wind tunnel and numerical study of a small vertical axis wind turbine, Renew. Energy 35 (2010) 412–422.
[15] M. Bhutta, N. Hayat, A. Farooq, Z. Ali, S. Jamil, Z. Hussain, Vertical axis wind turbine - a review of various configurations and design techniques, Renew. Sustain. Energy Rev. 16 (2012) 1926–1939.
[16] M. Hand, D. Simms, L. Fingersh, D. J. J. Cotrell, S. Schreck, S. Larwood, Unsteady Aerodynamics Experiment Phase VI: Wind Tunnel Test Configurations and Available Data Campaigns, NREL/TP-500–29955.
[17] R. Sheldahl, B. Blackwell, Free-air Performance Tests of a 5-metre-diameter Darrieus Turbine, SAND77–1063.
[18] M. Worstell, Aerodynamic Performance of the 17 Meter Diameter Darrieus Wind Turbine, SAND78–1737.
[19] R. Sheldahl, P. Klimas, L. Feltz, Aerodynamic Performance of a 5-metre-diameter Darrieus Turbine with Extruded Aluminum NACA-0015 Blades, SAND80–0179.
[20] R. Sheldahl, Comparison of Field and Wind Tunnel Darrieus Wind Turbine Data, SAND80–2469.
[21] M. Worstell, Aerodynamic Performance of the 17 Meter Diameter Darrieus Wind Turbine in the Three-bladed Configuration: an Addendum, SAND79–1753.
[22] B. Blackwell, R. Sheldahl, F. L.V., Wind Tunnel Performance Data for the Darrieus Wind Turbine with NACA 0012 Blades, SAND76–0130.
[23] ESDU, Blockage Corrections for Bluff Bodies in Confined Flows, Regent Street, London (UK), 1980.
[24] R. Mikkelsen, J. Sørensen, Modelling of wind tunnel blockage, Proceedings of the 2002 Global Windpower Conference and ExhibitionParis (FR).
[25] R. Mikkelsen, reportActuator Disc Methods Applied to Wind Turbines, Ph.D. ThesisTechnical University of Denmark.
[26] J. Sørensen, W. Shen, R. Mikkelsen, Wall correction model for wind tunnels with open test section, AIAA J. 44 (8) (2006) 1890–1894.
[27] Battisti, L. Zanne, S. Dell'Anna, V. Dossena, G. Persico, B. Paradiso, Aerodynamic measurements on a vertical axis wind turbine in a large scale wind tunnel, J. Energy Resour. Technol. 133.
[28] V. Dossena, G. Persico, B. Paradiso, L. Battisti, S. Dell'Anna, E. Benini, A. Brighenti, An experimental study of the aerodynamics and performance of a Vertical Axis Wind Turbine in confined and unconfined environment, ASME J. Energy Resour. Technol. 137.
[29] Y. Li, K. Tagawa, W. Liu, Performance effects of attachment on blade on a straight-bladed vertical axis wind turbine, Curr. Appl. Phys. 10 (2010) S335–S338.
[30] L. Battisti, E. Benini, A. Brighenti, S. Dell'Anna, M. Raciti Castelli, V. Dossena, G. Persico, U. Paulsen, T. Pedersen, Wind tunnel testing of the DeepWind demonstrator in design and tilted operating conditions, Energy 111 (2016) 484–497, https://doi.org/10.1016/j.energy.2016.05.080.
[31] G.V. Bussel, S. Mertens, H. Polinder, H. Sidler, The development of turby, a small VAWT for the built environment, in: Proceedings of the Global Wind Power Conference and Exhibition, 2004, pp. 28–31. Chicago (US).
[32] C. Ferreira, G. van Bussel, G. van Kuik, Wind tunnel hotwire measurements, flow visualization and thrust measurement of a VAWT in skew, J. Sol. Energy Eng. 128 (4) (2006) 487–497.
[33] C. Ferreira, G. van Bussel, F. Scarano, 2D PIV visualization of dynamic stall on a vertical Axis wind turbine, 45th AIAA Aerospace Sciences MeetingReno, Nevada (US).
[34] S. Tullis, A. Fiedler, K. McLaren, S. Ziada, Medium-solidity vertical Axis wind turbines for use in urban environments, VII World Wind Energy Association ConferenceKingston (CA).
[35] A. Fiedler, S. Tullis, Blade offset and pitch effects on a high solidity vertical Axis wind turbine, Wind Eng. 33 (3) (2009) 237–246.
[36] M. Takao, H. Kuma, T. Maeda, Y. Kamada, M. Oki, A. Monoda, A straight-bladed vertical Axis wind turbine with a directed guide vane row - effect of guide vane geometry on the performance, J. Therm. Sci. 18 (1) (2009) 54–57.
[37] S. Armstrong, A. Fiedler, S. Tullis, Flow separation on a high Reynolds number, high solidity vertical axis wind turbine with straight and canted blades and canted blades with fences, Renew. Energy 41 (2012) 13–22.
[38] L. Danao, O. Eboibi, R. Howell, An experimental investigation into the influence of unsteady wind on the performance of a vertical axis wind turbine, Appl. Energy 107 (2013) 403–411.
[39] Q. Li, T. Maeda, Y. Kamada, J. Murata, T. Kawabata, K. Furukawa, Analysis of aerodynamic load on straight-bladed vertical Axis wind turbine, J. Therm. Sci.

23 (4) (2014) 315–324.
[40] G. Tescione, D. Ragni, C. He, C.S. Ferreira, G. van Bussel, Near wake ow analysis of a vertical axis wind turbine by stereoscopic particle image velocimetry, Renew. Energy 70 (2014) 47–61.
[41] H. Peng, H. Lam, C. Lee, Investigation into the wake aerodynamics of a ve-straight-bladed vertical axis wind turbine by wind tunnel tests, J. Wind Eng. Ind. Aerod. 155 (2016) 23–35.
[42] F. Trivellato, L. Battisti, G. Miori, The ideal power curve of small wind turbines from field data, J. Wind Eng. Ind. Aerod. 107–108 (2012) 263–273.
[43] M. Raciti Castelli, G. Ardizzon, L. Battisti, E. Benini, G. Pavesi, Modeling strategy and numerical validation for a darrieus vertical Axis micro-wind turbine, Proceedings of the ASME 1010 International Mechanical Engineering Congress and Exposition (IMECE 2010), Vancouver, British Columbia (CA).
[44] I. E. 13005, Guide to the Expression of Uncertainty in Measurement, May 1999.
[45] B. Kirke, L. Lazauskas, Enhancing the performance of vertical axis wind turbine using a simple variable pitch system, Wind Eng. 15 (1991) 187–195.
[46] A. Bianchini, L. Ferrari, S. Magnani, Start-up behavior of a three-bladed H-Darrieus VAWT: experimental and numerical analysis, in: Proceedings of the ASME Turbo Expo, 2011, pp. 6–10.
[47] A. Rossetti, G. Pavesi, Comparison of different numerical approaches to the study of the H-Darrieus turbines start-up, Renew. Energy 50 (2013) 7–19.
[48] I. Paraschivoiu, Wind Turbine Design: with Emphasis on Darrieus Concept, Polytechnic International PressISBN 9782553009310.
[49] N. Fujisawa, S. Shibuya, Observations of dynamic stall on Darrieus wind turbine blades, J. Wind Eng. Ind. Aerod. 89 (2) (2001) 201–214.